

# Frequency dependence and vertical structure of ocean surface kinetic energy from global high-resolution models and surface drifter observations

Brian K. Arbic<sup>1,\*</sup>, Shane Elipot<sup>2,\*</sup>, Jonathan M. Brasch<sup>3</sup>, Dimitris Menemenlis<sup>4</sup>, Aurélien L. Ponte<sup>5</sup>, Jay F. Shriver<sup>6</sup>, Xiaolong Yu<sup>5</sup>, Edward D. Zaron<sup>7</sup>, Matthew H. Alford<sup>8</sup>, Maarten C. Buijsman<sup>9</sup>, Ryan Abernathey<sup>10</sup>, Daniel Garcia<sup>3</sup>, Lingxiao Guan<sup>3</sup>, Paige E. Martin<sup>10,11</sup>, Arin D. Nelson<sup>1,12</sup>

\*These authors contributed equally to this study.

<sup>1</sup>Department of Earth and Environmental Sciences, University of Michigan, Ann Arbor, MI, USA

<sup>2</sup>Rosenstiel School of Marine and Atmospheric Science, University of Miami, Miami, FL, USA

<sup>3</sup>Department of Electrical Engineering and Computer Science, University of Michigan, Ann Arbor, MI,

USA

<sup>4</sup>Jet Propulsion Laboratory, California Institute of Technology, Pasadena, CA, USA

<sup>5</sup>Ifremer, Université de Brest, CNRS, IRD, Laboratoire d'Océanographie Physique et Spatiale, IUEM,

Brest, France

<sup>6</sup>Naval Research Laboratory, Stennis Space Center, Mississippi, USA

<sup>7</sup>College of Earth, Ocean, and Atmospheric Sciences, Oregon State University, Corvallis, OR, USA

<sup>8</sup>Scripps Institution of Oceanography, University of California San Diego, La Jolla, California, USA

<sup>9</sup>School of Ocean Science and Engineering, University of Southern Mississippi, Stennis Space Center,

Mississippi

<sup>10</sup>Lamont-Doherty Earth Observatory, Columbia University, New York City, NY, USA

<sup>11</sup>Department of Physics, University of Michigan, Ann Arbor, MI, USA

<sup>12</sup>Graduate School of Oceanography, University of Rhode Island, Kingston, RI, USA

## Key Points:

- We examine global maps, frequency content, and vertical structure of ocean near-surface kinetic energy with drifter data and two models.
- Modeled near-inertial and tidal kinetic energy values are sensitive to wind forcing frequency and parameterized damping, respectively.
- Models capture latitude- and frequency-dependence in observed ratio of zonally averaged 0 to 15 m depth kinetic energy reasonably well.

---

Corresponding author: Brian K. Arbic & Shane Elipot, [arbic@umich.edu](mailto:arbic@umich.edu) & [selipot@rsmas.miami.edu](mailto:selipot@rsmas.miami.edu)

31 **Abstract**

32 The geographical variability, frequency content, and vertical structure of near-surface  
 33 oceanic kinetic energy (KE) are important for air-sea interaction, marine ecosystems, op-  
 34 erational oceanography, pollutant tracking, and interpreting remotely sensed velocity mea-  
 35 surements. Here, KE in high-resolution global simulations (HYbrid Coordinate Ocean  
 36 Model; HYCOM, and Massachusetts Institute of Technology general circulation model;  
 37 MITgcm), at the sea surface (0 m) and 15 m, are respectively compared with KE from  
 38 undrogued and drogued surface drifters. Global maps and zonal averages are computed  
 39 for low-frequency (periods longer than 2 days), near-inertial, diurnal, and semi-diurnal  
 40 bands. In the low-frequency band, near the equator, both models exhibit KE values that  
 41 are too low relative to drifters. MITgcm near-inertial KE is too low, while HYCOM near-  
 42 inertial KE lies closer to drifter KE, probably due to more frequently updated atmospheric  
 43 forcing. In the semi-diurnal band, MITgcm KE is too high, while HYCOM lies closer  
 44 to drifters, likely due to the inclusion of a parameterized topographic internal wave drag.  
 45 We assess the KE vertical structure by considering the ratio of zonally averaged KE in  
 46 0 m/15 m model results and undrogued/drogued drifter results. Over most latitudes and  
 47 frequency bands, model ratios track the drifter ratio to within error bars. All frequency  
 48 bands except the semi-diurnal band display measurable vertical structure. Latitudinal  
 49 dependence in the vertical structure is greatest in the diurnal and low-frequency bands.  
 50 As in a previous comparison of HYCOM and MITgcm to current meter observations,  
 51 HYCOM generally displays larger spatial correlations with the drifter observations than  
 52 MITgcm does.

53 **Plain Language Summary**

54 It is important to map and understand ocean surface currents because they affect  
 55 climate and marine ecosystems. Recent advances in global ocean models include the ad-  
 56 dition of astronomical tidal forcing alongside atmospheric forcing, and the advent of ever-  
 57 more-powerful computers that can resolve ever-finer features. Consequently, high-resolution  
 58 global models that include tidal forcing can simulate several types of oceanic motions  
 59 with some degree of realism. Here we evaluate ocean surface currents in high-resolution  
 60 simulations of two different ocean models through comparison with observations from  
 61 surface drifting buoys. We examine near-inertial motions, forced by fast-changing winds,  
 62 semi-diurnal tides, forced by the astronomical tidal potential, diurnal motions, arising  
 63 from tidal and other sources, and low-frequency currents and eddies, forced by atmospheric  
 64 fields. Global patterns in the models and drifters are broadly consistent. The two mod-  
 65 els differ in their degree of proximity to drifter measurements in the near-inertial band,  
 66 most likely due to different update intervals for atmospheric forcing, and in the semi-  
 67 diurnal band, most likely due to different damping schemes. The vertical structure of  
 68 the currents, as measured by drifter flows at the surface vs. 15 meters depth, is tracked  
 69 reasonably well by the models, although differences are found in some frequency bands.

70 **1 Introduction**

71 Oceanic surface currents are relevant for a range of multi-disciplinary scientific top-  
 72 ics and operational applications (Elipot & Wenegrat, 2021). For instance, surface cur-  
 73 rents are major actors in two crucial components of the climate system, the air-sea tran-  
 74 sition zone (Cronin & Coauthors, 2019) and marine ecosystems (Lévy et al., 2018). Maps  
 75 of surface currents are useful for understanding ocean dynamics, assessing operational  
 76 ocean modeling, enabling search-and-rescue missions, and tracking oil spills, plastics, and  
 77 other marine pollutants. Many of these applications, including predicting Lagrangian  
 78 trajectories of water parcels in the near-surface ocean, understanding air-sea transfer,  
 79 and others, require knowledge not only of currents but also their vertical structure near  
 80 the oceanic surface (Olascoaga et al., 2020).

Despite the importance of near-surface currents, not enough is known about their space-time variability. Here, we examine geographical maps, frequency content, and vertical structure of near-surface velocity variance (KE), in two different high-resolution global ocean models and in observations from NOAA's Global Drifter Program (GDP). Our quantification of vertical structure on a global scale is novel. The three-way comparison between two models and drifter observations points towards improvements that need to be made in the models and in interpretations of drifter data.

Mapping near-surface oceanic currents on a global scale is a formidable task. Quantifying high-frequency motions such as near-inertial flows (e.g., Pollard & Millard, 1970; Alford, 2003a, 2003b; Furuichi et al., 2008; Chaigneau et al., 2008; Simmons & Alford, 2012), semi-diurnal and diurnal tides, and the internal gravity wave continuum (Garrett & Munk, 1975) requires high-frequency sampling (e.g., at approximately hourly intervals). Time series from moored current meters can be used to separate high-frequency motions from lower-frequency motions including Ekman flows, mesoscale eddies, and the oceanic general circulation. Another advantage of mooring lines is the delivery of observations below the ocean surface. However, moored data are expensive to deploy and are available only at a relatively small number of geographical locations (see, e.g., Figure 1 of Luecke et al., 2020). Global-scale surface currents can be computed from satellite altimeter measurements of sea-surface height (SSH), providing that tides are removed and the geostrophic assumption is applied to the tide-corrected SSH fields. However, altimetry cannot detect near-inertial or Ekman flows, due to the negligible SSH signal in these motions. Altimetry measurements are also infrequent in time; the repeat time of the TOPEX/Jason series, for instance, is about 10 days. The geostrophic velocities computed from altimetry leave out high-frequency contributions to the velocity and hence KE fields.

The drifting buoys, or drifters, of the GDP (Lumpkin et al., 2017) yield a global dataset of near-surface ocean velocity in situ estimates. The drifter dataset allows for division of KE into several frequency bands, e.g., low-frequency, near-inertial, diurnal, and semi-diurnal, and has been used in many previous studies of oceanic flows. Maximenko et al. (2009) mapped the mean dynamic topography with drifters. Eliot and Gille (2009) used drifters to examine Ekman flows in the Southern Ocean. Thoppil et al. (2011) found relatively close agreement in low-frequency KE between high-resolution global simulations of the HYbrid Coordinate Ocean Model (HYCOM; Chassignet et al., 2009), the backbone operational model of the US Navy, and drifters. Recently, drifters have also been used to quantify high-frequency motions such as tides (Poulain & Centurioni, 2015). Kodaira et al. (2015) compared  $M_2$  tidal currents in a multi-layer tide model (without atmospheric forcing) to currents inferred from drifters. Zaron and Eliot (2021) found generally good agreement between tidal currents in satellite-altimetry constrained tidal models and drifters. Eliot et al. (2016) derived an hourly drifter product and demonstrated that it resolves motions at a wide range of frequencies. Yu et al. (2019) compared KE, over various low- and high-frequency bands, from the hourly drifter dataset and output from a high-resolution Massachusetts Institute of Technology general circulation model (MITgcm; Marshall et al., 1997) simulation, designated as LLC4320 and described in more detail in section 2.2.

The model-data comparison in Yu et al. (2019), performed over a wide range of frequency bands, was made possible by the emergence of a new class of high-resolution global ocean models that simultaneously include astronomical tidal forcing and atmospheric forcing (e.g., Arbic et al., 2010, 2012, 2018; Buijsman et al., 2020; Müller et al., 2012; Waterhouse et al., 2014; Rocha, Chereskin, et al., 2016; Rocha, Gille, et al., 2016). In these models, internal tides and mesoscale eddies co-exist and interact (Shriver et al., 2014; Buijsman et al., 2017; Nelson et al., 2019). As shown first in Müller et al. (2015) and later in other studies (e.g., Rocha, Chereskin, et al., 2016; Savage et al., 2017a, 2017b; Qiu et al., 2018; Torres et al., 2018; Luecke et al., 2020), such models are beginning to partially

133 resolve the internal gravity wave (IGW) continuum (Garrett-Munk spectrum; Garrett  
 134 & Munk, 1975).

135 Global IGW models, especially HYCOM and MITgcm LLC4320, have been widely  
 136 used by the community, to plan for field campaigns (e.g., J. Wang et al., 2018), under-  
 137 stand interactions between motions at different length and time scales (e.g., Pan et al.,  
 138 2020), and provide boundary forcing for higher-resolution regional models (Nelson et al.,  
 139 2020). HYCOM and MITgcm LLC4320 have been used to quantify the relative contribu-  
 140 tions of low- and high-frequency motions to SSH and KE as a function of geograph-  
 141 ical location (e.g., Richman et al., 2012; Savage et al., 2017a, 2017b; Rocha, Chereskin,  
 142 et al., 2016; Rocha, Gille, et al., 2016; Qiu et al., 2018; Torres et al., 2018). The ener-  
 143 getics of different classes of oceanic motions are of interest in their own right (Ferrari &  
 144 Wunsch, 2009). Global IGW models offer the potential for examining energy exchanges  
 145 between different classes of oceanic motions, as has been seen in observations (Le Boyer  
 146 & Alford, 2020). Quantitative mapping of low- and high-frequency motions is important  
 147 for satellite missions including the Surface Water Ocean Topography (SWOT) mission  
 148 (Morrow et al., 2019), planned for launch in 2022, which will measure SSH at high res-  
 149 olution in two-dimensional swaths. Remote sensing missions focused on measuring near-  
 150 surface ocean velocities, such as the existing airborne Sub-Mesoscale Ocean Dynamics  
 151 Experiment (S-MODE) mission (Rodriguez et al., 2020), the proposed Sea surface KIne-  
 152 matics Multiscale monitoring mission (SKIM; Ardhuijn et al., 2019) and the proposed  
 153 Winds And Currents Mission (WACM; Rodriguez et al., 2020), will benefit from quan-  
 154 tification of high- and low-frequency KE as well.

155 Because HYCOM and MITgcm LLC4320 are widely used, it is important to com-  
 156 pare these models to observations. A summary of early model comparisons of HYCOM  
 157 and MITgcm LLC4320 tidal simulations with observations is provided in Arbic et al. (2018).  
 158 Up to that point, HYCOM, and to a lesser extent MITgcm LLC4320, had been compared  
 159 to time-series observations from moored instruments, and global maps of SSH from satel-  
 160 lite altimetry. IGW results from MITgcm LLC4320 have also been compared to along-  
 161 track Acoustic Doppler Current Profiler (ADCP) data (Rocha, Chereskin, et al., 2016;  
 162 Chereskin et al., 2019).

163 This paper uses model and drifter comparisons to focus on the geographic variabil-  
 164 ity, frequency content, and vertical structure of near-surface KE. Yu et al. (2019) showed  
 165 that LLC4320 semi-diurnal tidal KE was too strong, and near-inertial KE too weak, rel-  
 166 ative to drifter observations. Here, we build upon the Yu et al. (2019) study through inter-  
 167 comparison of HYCOM, MITgcm LLC4320, and drifters. The HYCOM and MITgcm  
 168 LLC4320 simulations differ in several respects, and we anticipate that they will perform  
 169 differently in comparisons to drifters. We especially anticipate differences in the near-  
 170 inertial bands, due to more frequent updates of the wind fields in HYCOM (3 hours) rel-  
 171 ative to MITgcm LLC4320 (6 hours), and in the semi-diurnal tidal band, due to the lack  
 172 of a parameterized topographic wave drag in MITgcm LLC4320. In HYCOM simula-  
 173 tions, a parameterized topographic internal wave drag is included in order to roughly ac-  
 174 count for the damping of tidal motions due to breaking small-scale internal tides that  
 175 are unresolved in global models (Arbic et al., 2010, 2018; Ansong et al., 2015; Buijsman  
 176 et al., 2016, 2020). Ansong et al. (2015) demonstrated that the SSH signature of inter-  
 177 nal tides in HYCOM is closer to altimetry observations when the HYCOM simulations  
 178 contain a wave drag than when they do not contain a wave drag. Here we examine the  
 179 impact of including wave drag (as in HYCOM) vs. excluding it (as in LLC4320) on near-  
 180 surface semi-diurnal KE. A better quantification of the vertical structure of near-surface  
 181 currents will aid our understanding of the air-sea exchange of heat, momentum, and gases,  
 182 and of the dispersal of pollutants and biologically important tracers (Eliot & Wenegrat,  
 183 2021). The vertical structure of velocity has important implications for the ongoing S-  
 184 MODE airborne mission and proposed satellite missions focusing on surface ocean ve-  
 185 locity measurements (Ardhuin et al., 2019; Rodriguez et al., 2020). These missions will

need information on the frequency dependence of vertical structure in order to interpret the implications of surface current measurements for subsurface oceanic conditions (J.T. Farrar, personal communication, 2021).

To our knowledge, a detailed global examination of the vertical structure of near-surface KE, for both high- and low-frequency motions, has not been done before. As in Yu et al. (2019), we use both undrogued and drogued drifters which provide estimates of oceanic velocity at 0 m (sea surface) and 15 m, respectively. Accordingly, we compare model results at 0 m to undrogued drifter results, and model results at 15 m to drogued drifter results. We also compute the ratio of zonally averaged KE in undrogued drifters to zonally averaged KE in drogued drifters, and compare the drifter ratio to the ratio of zonally averaged 0 m KE to zonally averaged 15 m KE in the models. Error bars on the drifter ratios are large, especially for near-inertial and tidal motions, and windage (erroneous slips of water past drifters) are a known problem in undrogued drifter observations (Section 2.3). Nevertheless, clear vertical structure is seen in all of the frequency bands except the semi-diurnal band, and the model ratios, which suffer from completely different biases and errors, follow the drifter ratio over most latitudes and most frequency bands. We provide some discussion on the causes of the vertical structure. The vertical structure of the diurnal band is especially interesting because of the multiple forcing mechanisms in this band (diurnal tides, wind-forced near-inertial waves which overlap with the diurnal band near 30° latitude, and diurnal cycling of Ekman and submesoscale flows).

## 2 Data and Methods

### 2.1 HYCOM simulation

The global HYCOM simulations employ nominal 1/25° horizontal grid spacing and 41 hybrid layers (Bleck, 2002) covering the vertical direction. HYCOM employs terrain-following coordinates in shallow waters, and isopycnal coordinates in the subsurface open-ocean. In the near-surface open-ocean, the uppermost 14 layers are in z-mode, with seven z-levels, having spacing ranging from 1.00 to 6.87 m, in the uppermost 30 m. The HYCOM “0 m” (surface) results actually represent the mid-point of the uppermost layer. The HYCOM “15 m” results represent interpolations to 15 m. The interpolation largely reflects results from the HYCOM level at 13.185 m, which lies in between adjacent levels at 8.38 and 18.55 m; the latter three depth values represent mid-depth points of the respective vertical layers in which they lie. HYCOM employs the widely used K profile parameterization (KPP) scheme (Large et al., 1994) for vertical mixing. Atmospheric forcing fields from the U.S. Navy Global Environmental Model (Hogan et al., 2014) are applied every three hours. We use a 360-day record of hourly snapshots of surface and 15-meter horizontal velocity fields, starting on 1 January 2014, and produced with a 75 second baroclinic timestep.

HYCOM’s tidal forcing includes the two largest diurnal components ( $K_1$  and  $O_1$ ) and the three largest semi-diurnal components ( $M_2$ ,  $S_2$ , and  $N_2$ ). The self-attraction and loading (SAL) term is taken from the altimetry-constrained TPXO8 barotropic tide model (Egbert et al., 1994; Egbert & Erofeeva, 2002). The HYCOM parameterized topographic wave drag scheme, taken from Jayne and St. Laurent (2001), is tuned to minimize the  $M_2$  surface elevation errors with respect to TPXO8. Following Ngodock et al. (2016), an Augmented State Ensemble Kalman Filter (ASEnKF) reduces the area-weighted error of the surface tidal elevations, computed with respect to TPXO8 in waters deeper than 1000 m and latitudes equatorward of 66°, to 2.6 cm.

233            **2.2 MITgcm LLC4320 simulation**

234            LLC4320 is a global MITgcm simulation with nominal  $1/48^\circ$  horizontal grid spacing  
 235            and 90 vertical z-levels. There are 13 z-levels in the uppermost 30 m, with thickness  
 236            ranging from 1.0 to 4.6 m. The LLC4320 “15 m” velocities are taken from the 9th grid  
 237            cell from the surface, which spans 13.26 to 16.1 m depth. LLC4320 also employs the KPP  
 238            vertical mixing scheme. LLC4320 is forced by the full luni-solar astronomical tidal po-  
 239            tential and by six-hourly atmospheric fields from the  $0.14^\circ$  European Centre for Medium-  
 240            Range Weather Forecasting (ECMWF) operational model analysis, starting in 2011. The  
 241            LLC4320 baroclinic time step is 25 s. We use a year-long record of near-surface horizon-  
 242            tal velocity fields, saved as hourly snapshots and starting on 12 November 2011.

243            We have found that the tidal forcing in the LLC4320 simulation has been overes-  
 244            timated by a factor of 1.1121, while the self-attraction and loading (SAL) term (SAL;  
 245            Hendershott, 1972; Ray, 1998) has been inadvertently omitted. With the aid of a barotropic  
 246            tide model, we have estimated that these implementation errors in MITgcm LLC4320  
 247            yield a barotropic semi-diurnal tidal KE that is too high by a factor of 1.17 (Michael Schin-  
 248            delegger, personal communication, 2020). Diurnal tidal KE in MITgcm LLC4320 is also  
 249            expected to be affected by the implementation of astronomical forcing. These results will  
 250            be reported in detail elsewhere. In the results shown here, the LLC4320 KE in semi-diurnal  
 251            and diurnal bands are not corrected. As noted above, the MITgcm LLC4320 simulations  
 252            do not employ a parameterized topographic wave drag.

253            **2.3 Ocean Surface Drifters**

254            In-situ estimates of ocean near-surface velocities are obtained from the NOAA’s  
 255            GDP (Lumpkin et al., 2017) which maintains an array of surface drifting buoys, currently  
 256            tracked by the Global Positioning System and previously by the Argos system. We use  
 257            version 1.04c of the hourly high-frequency dataset (Eliopot et al., 2016) containing 17,324  
 258            individual surface drifter trajectories from October 1987 to June 2020, totalling  $\sim 166\text{M}$   
 259            estimates of hourly positions and velocities. The spatial coverage of the drifter dataset  
 260            is global, yet inhomogeneous with higher data density in convergence zones in the mid-  
 261            dle of ocean gyres and sparse observations at the equator due to Ekman divergence, which  
 262            tends to disperse drifters away (Eliopot et al., 2016).

263            Drifter data are intrinsically Lagrangian, in contrast to the Eulerian model out-  
 264            put that we compare to the drifter results. Nevertheless, segments of velocity time se-  
 265            ries from drifters are considered to estimate kinetic energy locally; we assign the mean  
 266            geographical position of a trajectory segment to each estimate before bin averaging. La-  
 267            grangian sampling leads to spectral smearing as drifters convolve spatial and temporal  
 268            oceanic variability (Yu et al., 2019; Zaron & Eliopot, 2021). Lagrangian spectra have lower  
 269            and wider tidal peaks, which do not stand above the background as much as peaks in  
 270            Eulerian spectra do. In addition, tidal lines in both Lagrangian and Eulerian spectra widen  
 271            due to interaction with currents and eddies, which renders the tides less coherent or sta-  
 272            tionary (e.g., Ray & Zaron, 2011; Shriver et al., 2014; Zaron & Egbert, 2014; Ponte &  
 273            Klein, 2015; Kerry et al., 2016; Buijsman et al., 2017; Savage et al., 2017a; Zaron, 2017;  
 274            Nelson et al., 2019).

275            We utilize both drogued and undrogued drifter data, in waters deeper than 500 m.  
 276            Drogued drifter displacements, which comprise 48% of the trajectories in the dataset,  
 277            are expected to be representative of ocean velocity at 15-m depth with an estimated er-  
 278            roneous slip of the water past the drifter of  $0.7 \text{ cm s}^{-1}$  downwind per  $10 \text{ m s}^{-1}$  wind speed  
 279            (Niiler & Paduan, 1995). Undrogued drifters, which comprise 52% of the dataset, are  
 280            expected to represent ocean velocities at the surface (0 m), but with a slip of an order  
 281            of magnitude larger compared to drogued drifters [ $8.6 \text{ cm s}^{-1}$  per  $10 \text{ m s}^{-1}$  wind speed,  
 282            (Lumpkin & Pazos, 2007)]. As such, undrogued drifter observations likely exhibit larger  
 283            downwind velocity errors but these are yet to be comprehensively distinguished from real

oceanic processes. For example, locally wind-driven velocities at the surface are more energetic than at 15-m depth because of vertical shear at a broad range of frequencies through Ekman dynamics (Elipot & Gille, 2009; Lilly & Elipot, 2021), or through surface gravity wave processes and their associated Stokes drift (Polton et al., 2005). Yet, undrogued drifters qualitatively capture the same KE features as drogued drifters (Yu et al., 2019). In particular, as shown by Yu et al. (2019) and further confirmed here, results are nearly identical in the semi-diurnal band, suggesting that a correction for the wind slip or an adequate assessment of its magnitude would need to be informed by an unknown dependency on frequency and to take into account the entire frequency spectrum of the observable wind forcing. In addition, typical estimation errors for the hourly drifter velocity estimates (Elipot et al., 2016) are between 2 and 5 cm s<sup>-1</sup> (see Figure S2 of Yu et al., 2019) with unknown frequency distribution. As such, a comprehensive assessment of the velocity errors from drogued and undrogued drifters, and how these errors affect kinetic energy estimates in various frequency bands, is beyond the scope of this study. The general agreement of the vertical structure ratio in models and drifters, seen in spatial maps and zonal averages, supplies some confidence that the vertical structure ratio computed from drifters is meaningful, noisy though it may be.

#### 2.4 Frequency Rotary Spectra

As in Yu et al. (2019), we compute frequency rotary spectra (Gonella, 1972; Mooers, 1973) of model and drifter velocities. Frequency rotary spectra allow us to decompose velocity variance as a function of frequency, and to separate clockwise versus counterclockwise motions. This clockwise vs. counterclockwise separation is especially important in the case of near-inertial oscillations. Velocity time series are split into 60-day segments overlapping by 50%, detrended, and multiplied by a Hann window. The discrete Fourier transform of  $u+iv$ , where  $u$  and  $v$  respectively denote the zonal and meridional velocity components, is then computed for each segment. The Fourier coefficients are multiplied by their complex conjugates to form spectral estimates which are then averaged over segments and multiplied by a factor that accounts for variance lost to the Hann window operation. Following Yu et al. (2019), the velocity variance, which is decomposed as a function of frequency in the spectra, is interpreted as kinetic energy; no factor of 1/2 is included in our KE calculations.

Also as in Yu et al. (2019), the rotary spectra are integrated over specific frequency bands: semi-diurnal ( $\pm[1.9, 2.1]$  cpd), diurnal ( $\pm[0.9, 1.1]$  cpd), high frequency ( $> 0.5$  cpd and  $< -0.5$  cpd), and near-inertial ( $\pm[0.9, 1.1]f$ , where  $f$  is Coriolis frequency). Low-frequency kinetic energy is taken as total kinetic energy, computed as the time-mean of the squares of the zonal velocity time series plus the time-mean of the squares of the meridional velocity time series, minus high-frequency kinetic energy, the latter computed from the spectra.

Our definitions of the bands present some challenges for near-inertial motions. First, the near-inertial band as defined above covers only the “local” near-inertial KE. Near-inertial motions, like low-mode internal tides, can propagate over long distances (Alford, 2003a; Simmons & Alford, 2012), and in such cases their frequency is no longer equal to the local value of  $f$ . Second, our analysis, like that of Yu et al. (2019), does not distinguish between near-inertial and diurnal motions where the definitions of these bands overlap, namely, within 24.1–37.5° of latitude.

### 3 Results

In order to characterize KE and its vertical structure, we consider zonally and globally averaged velocity rotary spectra (Elipot & Lumpkin, 2008), geographical 1° by 1° maps of KE calculated by integrating spectra over the frequency bands defined earlier, and zonal averages of these KE maps. Thus, all of the results shown in this paper rep-

334 resent spatial averages. To reduce computational time, model outputs are first subsampled  
 335 on  $1/4^\circ$  grids (without performing any spatial averaging) before computing spectra  
 336 and applying spatial averaging. Spatial averages are only computed when more than  
 337 50% of the points in a  $1^\circ$  by  $1^\circ$  bin are deeper than 500 m, and shallower gridpoints are  
 338 discarded in the computation. The drifter averages are computed in a similar manner.

339 Zonally-averaged rotary spectra for undrogued and drogued drifters, and at 0 m  
 340 and 15 m in the models, visualized as a function of frequency and latitude, display rel-  
 341 atively similar KE levels and structures (Figure 1). Peaks corresponding to diurnal fre-  
 342 quencies (near  $\pm 1$  cpd) and semi-diurnal frequencies (near  $\pm 2$  cpd), and a large low-  
 343 frequency continuum (near 0 cpd) are evident in all six subplots. Ridges of near-inertial  
 344 energy, which follow the negative of the Coriolis frequency, from  $\sim -1.7$  cpd at  $60^\circ\text{N}$  to  
 345  $\sim 1.7$  cpd at  $60^\circ\text{S}$ , are also evident in all six subplots of Figure 1. Near  $30^\circ$  latitude, the  
 346 inertial ridge overlaps with the diurnal peaks in the anticyclonic domain (at negative fre-  
 347 quencies in the northern hemisphere, and positive frequencies in the southern hemisphere).  
 348 The low-frequency peak, around zero cycles per day, is broader in frequency in the drifters  
 349 than in the models. The models exhibit semi-diurnal tidal peaks that rise above the back-  
 350 ground more dramatically than the peaks in the drifter spectra. The models also dis-  
 351 play a “peaky” or “picket fence” distribution of energy at high-frequency tidal har-  
 352 monics, with little energy in between the harmonics, as noted in previous studies (e.g., Müller  
 353 et al., 2015; Savage et al., 2017b). In contrast, the drifter tidal peaks do not stand out  
 354 above the background as strongly as in the models, as discussed earlier and in Zaron and  
 355 Elipot (2021).

356 Another faint but striking feature of these latitude-frequency rotary spectra is the  
 357 presence of translated images of the near-inertial ridge at  $-f \pm 1, 2, 3$  cpd in both the  
 358 drifter spectra and in the model spectra. The model spectra additionally exhibit mir-  
 359 ror images of the inertial ridge at  $f \pm 0, 1, 2, 3$  cpd. These features were previously seen  
 360 in a similar figure in Yu et al. (2019) for drifters and MITgcm LLC4320, and for drifter  
 361 data only in Elipot et al. (2016) up to 12 cpd. Elipot et al. (2016) speculated that these  
 362 features may be representative of small departures from circular geometry for inertial  
 363 oscillations, or of triad interactions between near-inertial waves and internal waves at  
 364 tidal frequencies, but also noted that their magnitudes depended to some extent upon  
 365 the processing applied to the drifter data to obtain hourly velocity estimates. The fact  
 366 that these features are also observed in the models suggest that they might be represen-  
 367 tative of real, as yet uncharacterized, oceanic processes.

368 The relative energy levels in the different bands are more easily compared in glob-  
 369 ally averaged rotary spectra, for which the anticyclonic domain is assigned here to pos-  
 370 itive frequencies and the cyclonic domain to negative frequencies, as in the southern hemi-  
 371 sphere (Figure 2). The highest energy levels, associated with large-scale currents, mesoscale  
 372 eddies, and Ekman flows, are seen in high and wide peaks at low frequencies (around zero).  
 373 Whereas the near-inertial anticyclonic ridge is clearly visible in frequency-latitude spec-  
 374 tra (Figure 1), in globally averaged spectra, that ridge is instead spread unevenly between  
 375 0 and 1.7 cpd in the anticyclonic frequency domain, weighted by the latitudinal distri-  
 376 bution of the spectral estimates. As a result, energy levels are generally higher below the  
 377 semi-diurnal frequency band in the anticyclonic domain than in the cyclonic domain. Semi-  
 378 diurnal and diurnal tidal peaks are clearly visible in both the model and drifter spec-  
 379 tra but rise above the background much less in the drifter spectra than in the model spec-  
 380 tra, as is made especially clear in the insets of Figure 2. The insets illustrate the wider  
 381 and lower semi-diurnal tidal peaks in Lagrangian spectra in comparison to Eulerian spec-  
 382 tra. As noted earlier, in the higher frequency part (e.g.,  $> 2$  cpd) of the IGW contin-  
 383 uum, spectra are much peakier in the models, especially HYCOM. The IGW continuum  
 384 falls off more steeply in HYCOM than in MITgcm LLC4320, because of the lower res-  
 385 olution (coarser grid spacings) in HYCOM. The continuum is more elevated and smoother  
 386 in the drifter spectra, and displays a noise floor at 12 cpd which is about one decade higher

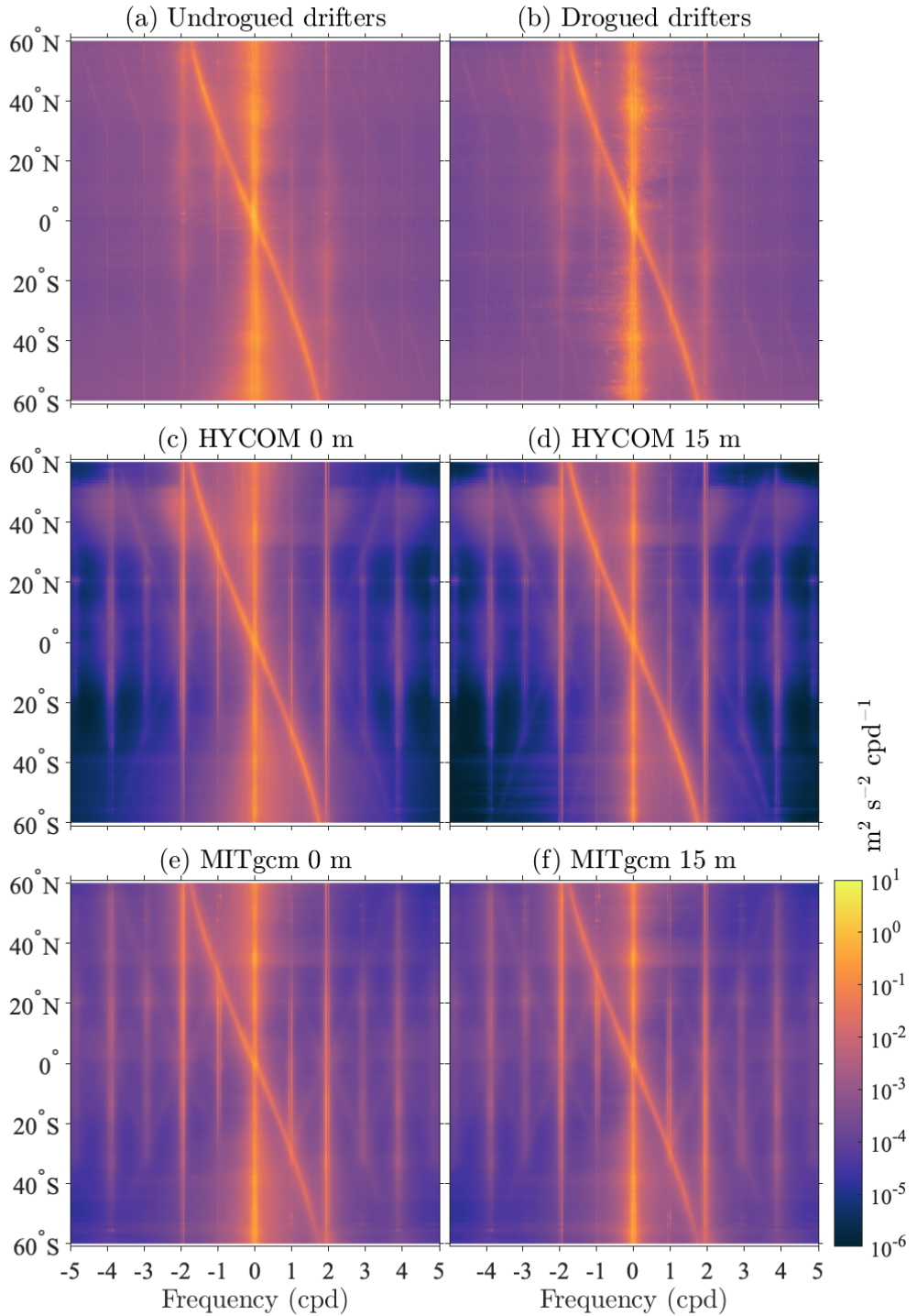


**Figure 1.** Zonally averaged rotary spectra of KE in  $1^\circ$  latitude bins between  $60^\circ\text{S}$  and  $60^\circ\text{N}$  for undrogued and drogued drifters (panels a and b), for HYCOM at 0 m and 15 m (panels c and d), and for MITgcm LLC4320 at 0 m and 15 m (panels e and f). Only frequencies between -5 and 5 cycle per day (cpd) are displayed. The frequency resolution is 1/60 cpd. The common decimal logarithmic color scale is displayed at the bottom right.

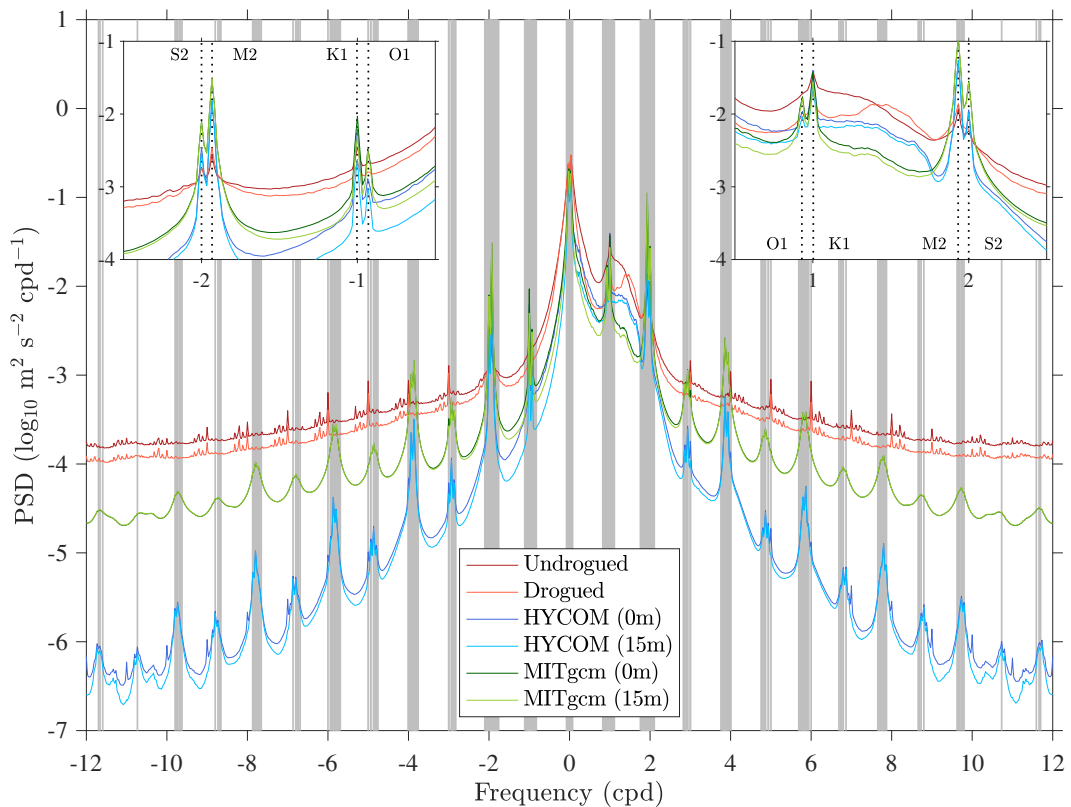


**Figure 2.** Globally averaged rotary spectra of KE from undrogued and drogued drifters (red curves), from 0 m and 15 m HYCOM (blue curves), and from 0 m and 15 m MITgcm LLC4320 (green curves). Anticyclonic and cyclonic frequencies are assigned to positive and negative frequencies, respectively. The vertical gray lines indicate 145 tidal frequencies in both positive and negative frequency domains. The two insets show the same spectra but with a focus on diurnal and semidiurnal anticyclonic frequencies (right) and cyclonic frequencies (left). The vertical dotted lines in the insets show the O<sub>1</sub>, K<sub>1</sub>, M<sub>2</sub>, and S<sub>2</sub> frequencies.

than MITgcm LLC4320, and more than two decades higher than HYCOM. This noise floor depends on the tracking-system for drifters: as shown by Yu et al. (2019), when only GPS-tracked drifters are considered instead of Argos-tracked drifters (Elipot et al., 2016), the spectral level and spectral slope at the highest frequencies for drifter spectra is in approximate agreement with MITgcm LLC4320 (see Figure 2 of Yu et al. (2019)). Many small but distinct spectral peaks that do not necessarily correspond to tidal constituents are seen in the drifter spectra for frequencies higher than 4 cpd. The amplitude and frequency of these peaks depend also on the drifter tracking system (see Figure 2 of Yu et al. (2019)) and may be artifacts of the estimation methods for drifter position and velocities (Elipot et al., 2016).

### 3.1 Low-frequency KE

Global maps of low-frequency KE highlight well-known large-scale currents and the mesoscale eddies they spawn, both of which are dominant in equatorial regions, western boundary current regions such as the Gulf Stream and Kuroshio, and the Antarctic Circumpolar Current (Figure 3, panels a-f). Low-frequency Ekman flows also contribute to these surface and near-surface patterns (Lumpkin & Johnson, 2013). At both

403 depth levels, HYCOM overestimates the drifter observations in the near-equatorial south-  
 404 Indian Ocean and in the Pacific off the Western coast of South America, while MIT-  
 405 gcm LLC4320 overestimates the drifters in the eastern North Atlantic Ocean and parts  
 406 of the Southern Ocean. MITgcm LLC4320 also features an incorrect positioning of the  
 407 Gulf Stream, which does not veer to the northeast as it does in HYCOM and the drifters.  
 408 The same Gulf Stream patterns were noted in surface velocities computed from satel-  
 409 lite altimetry in Luecke et al. (2020). Despite these local differences, the correlations be-  
 410 tween all these maps ( $\sim 0.70$ ) indicate the same level of global spatial agreement between  
 411 the results from drifters and the models on one hand, and between the results from two  
 412 models on the other hand.

413 Maps of the ratio of undrogued to drogued KE (Figure 3, panel g) and the ratio  
 414 of 0 m to 15 m KE in the models (Figure 3, panels h-i) display some similarities, despite  
 415 the noisiness inherent in the drifter map. The mid- to high-latitude northeast and south-  
 416 east Pacific Ocean, for instance, display relatively large values of the ratio in all three  
 417 maps. In the near-equatorial Pacific relatively low values of this ratio are seen in all three  
 418 maps. The spatial correlation between the model ratio maps (0.51) is significantly higher  
 419 than the spatial correlation between either model and the drifters. The HYCOM cor-  
 420 relation with the drifter ratio map (0.37) is slightly higher than the MITgcm LLC4320  
 421 correlation with the drifters (0.33).

422 Zonally averaged low-frequency KE in both models is generally comparable to, but  
 423 lower than, drifter KE (Figure 4, panels a and b). The models and drifters all exhibit  
 424 a peak of energy at the equator, but the peak values in HYCOM and especially MIT-  
 425 gcm LLC4320 are too low, the latter by a factor of about two. This disagreement be-  
 426 tween models and drifters near the equator should be interpreted with caution as the sam-  
 427 pling density from drifters near the equator is low (Figure 3, panels a and d). In the mid-  
 428 to high-latitudes of the southern hemisphere, MITgcm LLC4320 lies closer to drifter ob-  
 429 servations while HYCOM KE is too low. With the exception of the energetic peak near  
 430 35°N, over most mid- to high-latitudes in the northern hemisphere, both models are too  
 431 low.

432 The ratios of zonally averaged model 0 m KE to zonally averaged model 15 m KE  
 433 track the corresponding ratios in the drifters (zonally averaged undrogued drifter KE to  
 434 zonally averaged drogued drifter KE) reasonably well (to within error bars) over most  
 435 latitudes (Figure 4c). Maximum values of the KE ratio are seen at high latitudes in both  
 436 hemispheres in the drifters and in HYCOM, whereas MITgcm LLC4320 does not track  
 437 this high-latitude behavior. Neither model tracks the relatively high drifter ratios be-  
 438 tween about 15-30°S well. We speculate that the poor agreement in this latitude band  
 439 may be due to a relative lack of drogued drifter data in the South Pacific, which could  
 440 introduce a bias in the ratios. The greater energy in the undrogued drifters over most  
 441 latitudes (represented by values of the ratio greater than one) may be due in part to their  
 442 wind bias as noted earlier. However, the relative closeness of this KE ratio in results from  
 443 models, which do not suffer from a wind bias, to the drifter results suggests that wind  
 444 bias alone is unlikely to account for all of the vertical structure seen in Figure 4c.

### 445 3.2 Near-inertial KE

446 Near-inertial KE is generally larger in mid-to-high latitudes than it is near the equa-  
 447 tor for both observational and model results, with the largest values found in the north  
 448 Pacific (Figure 5, panels a-f), as shown in previous studies (e.g., Alford, 2003b; Chaigneau  
 449 et al., 2008; Eliot et al., 2010). Faint but distinct relative maxima of KE are evident  
 450 in the maps for the models around 30° where our analysis picks up tidal motions and  
 451 wind-driven inertial motions that are both near-diurnal at that latitude. MITgcm LLC4320  
 452 systematically underestimates the drifter results over most of the ocean, while HYCOM  
 453 is in generally better agreement though it still underestimates the drifter results in the

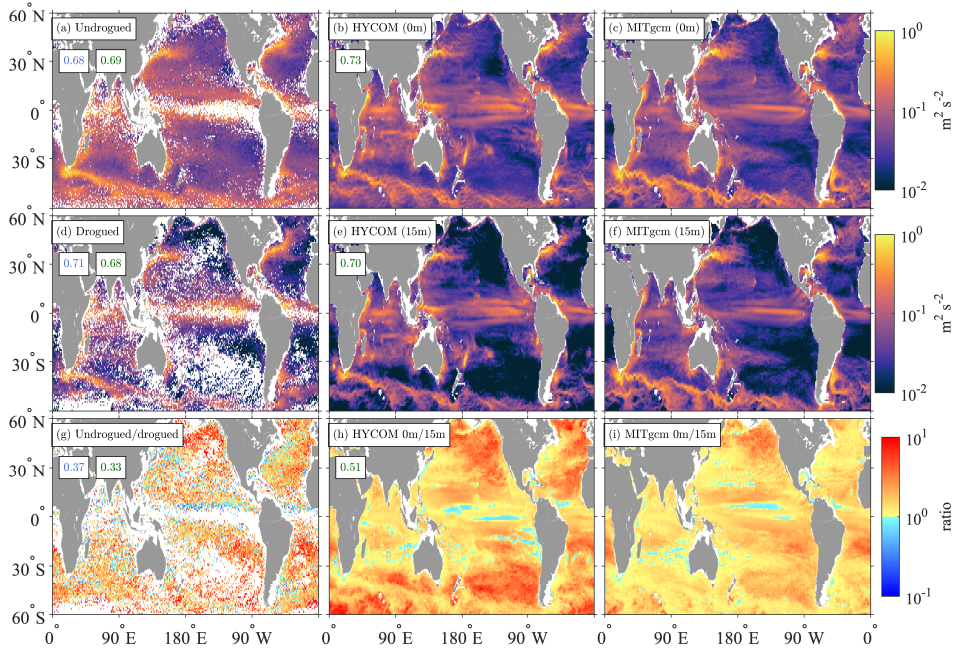


**Figure 3.** Global maps of low-frequency ( $> -0.5$  cpd and  $< 0.5$  cpd) kinetic energy (KE) from undrogued and drogued drifters (panels a and d), from HYCOM at 0 m and 15 m (panels b and e), and from MITgcm LLC4320 at 0 m and 15 m (panels c and f). The ratios of undrogued to drogued drifter KE, and 0 m to 15 m KE for the HYCOM and MITgcm LLC4320 simulations are shown in panels g, h, and i, respectively. Note the decimal logarithmic color scale for the ratio maps. The spatial correlations between the drifter maps and HYCOM and MITgcm LLC4320 maps are indicated in the upper left corners of panels a, d, and g, with HYCOM values in blue to the left of MITgcm LLC4320 values in green. The spatial correlations between HYCOM and MITgcm LLC4320 maps are indicated in the upper left corners of panels b, e, and h.

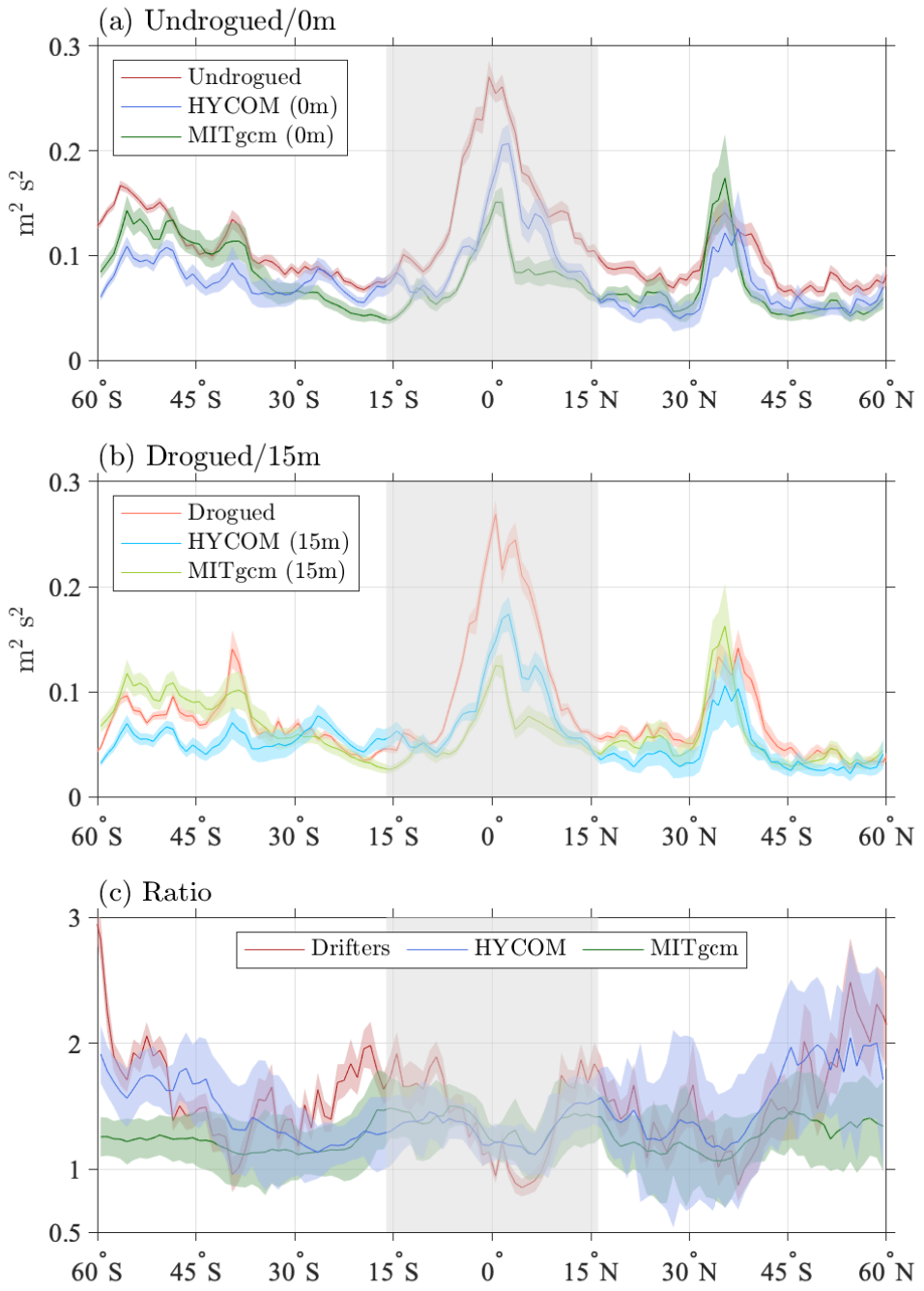


**Figure 4.** Zonally averaged low-frequency ( $> -0.5$  cpd and  $< 0.5$  cpd) kinetic energy (KE) from (a) undrogued drifters and 0 m model levels, and (b) drogued drifters and 15 m model levels. Ratios of zonal averages of undrogued/drogued drifter KE, and 0 m/15 m model KE, are shown in (c). The gray shaded region in each panel indicates the latitudes where the near-inertial and low-frequency bands exhibit some overlap (see Fig. 1). The shading around each curve corresponds to two standard errors of the calculated 1° zonal averages from the geographical maps.

454 northern Pacific. Near-inertial KE is conspicuously lacking in MITgcm LLC4320 over  
 455 the Antarctic Circumpolar Current south of 45°S. In both models, near meridional streaks  
 456 of near-inertial KE stand out, probably related to individual tropical cyclones and storms  
 457 present in the model forcing fields within their respective integration years. The drifter  
 458 maps do not show such features which should be averaged out by the many years of drifter  
 459 data used for this analysis. The different forcing years of the models and the multi-year  
 460 nature of the drifter dataset may explain why the spatial correlations between these maps  
 461 at both levels are lower than seen in, for instance, the low-frequency band; the two model  
 462 maps correlate at 0.60 at the surface and at 0.58 at 15 m depth. The drifter maps cor-  
 463 relate with the model maps at approximately equivalent levels, albeit slightly better in  
 464 HYCOM compared to MITgcm LLC4320 (0.60 versus 0.51 at the surface, and 0.54 ver-  
 465 sus 0.45 at 15 m).

466 The ratio maps for the two models appear similar but exhibit relatively low cor-  
 467 relation between them (0.48). They both indicate that near-inertial KE is slightly larger  
 468 at the surface compared to 15 m. Some unexplained discontinuities in these maps are  
 469 noticeable near 30° latitude which may be due to overlapping dynamical processes of a  
 470 different nature taking place there (tidal vs. wind-driven). The ratio map for the drifters  
 471 is extremely noisy, and exhibits very low correlation with the model ratio maps.

472 In the zonal averages (Figure 6), as anticipated from the global maps, near-inertial  
 473 KE is significantly higher in HYCOM than in MITgcm LLC4320, up to a factor larger  
 474 than 4.5 at 54.5° S at the surface and at 15 m. As noted before, this discrepancy in model  
 475 near-inertial KE levels may arise from the lower-frequency wind forcing in MITgcm LLC4320  
 476 (6 hours) compared to HYCOM (3-hour). Rimac et al. (2013) demonstrated that near-  
 477 inertial KE in models is highly sensitive to coupling period, with hourly forcing yield-  
 478 ing KE three times higher than 6-hourly forcing. Flexas et al. (2019) found relatively  
 479 low wind-power input to the near-inertial motions in MITgcm LLC4320, due to the 6-  
 480 hourly updates in the wind forcing. Near-inertial KE in HYCOM follows the drifters rel-  
 481 atively well in the northern hemisphere between about 10–30°N and in the southern hemi-  
 482 sphere. In the southern hemisphere, at the surface, the undrogued drifter near-inertial  
 483 KE is however systematically slightly higher than HYCOM, perhaps because of under-  
 484 estimated windage of the undrogued drifters within strong wind environments. In con-  
 485 trast, at 15-m depth, HYCOM is in closer agreement with the drogued drifters in the  
 486 southern hemisphere. At latitudes between about 35–60°N, HYCOM KE values, though  
 487 closer to the drifters than MITgcm LLC4320 values are, are still substantially lower than  
 488 the drifters. Separation of the zonal averages into basins demonstrates that the main cause  
 489 of the discrepancy is located in the North Pacific Ocean (Figure 7). The reasons for the  
 490 North Pacific discrepancy in HYCOM are unclear, but may be related in part to the 3-  
 491 hourly coupling period of the NAVGEM atmospheric model to HYCOM, which, though  
 492 more frequent than the 6 hour coupling period for MITgcm LLC4320, may still be in-  
 493 sufficiently frequent. Another potential cause of the discrepancy is that the model out-  
 494 puts are of one year duration, while the drifter data span multiple years. However, sep-  
 495 aration of the drifter data into different years (not shown) produced year-to-year differ-  
 496 ences in the zonal averages that are much smaller than the differences between the mod-  
 497 els and drifters seen in Figure 7a.

498 The ratios of zonally averaged undrogued to drogued drifter KE are still noisy, but  
 499 are consistently between about 1 and 2, except in a few latitude bands (Figure 6c). Over  
 500 most latitudes, the ratio of 0 m to 15 m KE in both models follows the drifter ratios rel-  
 501 atively well, within error bars. The model ratios are larger than one, but are generally  
 502 not much larger than one—values of 1.1 are typical.

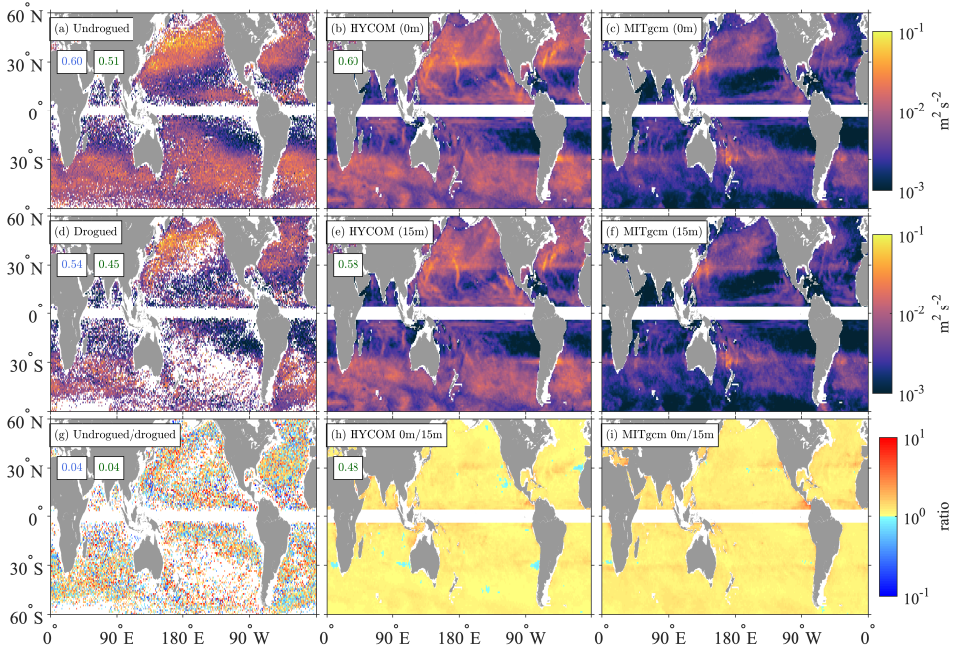


**Figure 5.** Global maps of near-inertial ( $\pm[0.9, 1.1]f$ ) KE from undrogued and drogued drifters (panels a and d), from HYCOM at 0 m and 15 m (panels b and e), and from MITgcm LLC4320 at 0 m and 15 m (panels c and f). The ratios of undrogued to drogued drifter KE, and 0 m to 15 m KE for the HYCOM and MITgcm LLC4320 simulations are shown in panels g, h, and i, respectively. Note the decimal logarithmic color scale for the ratio maps. The spatial correlations between the drifter maps and HYCOM and MITgcm LLC4320 maps are indicated in the upper left corners of panels a, d, and g, with HYCOM values in blue to the left of MITgcm LLC4320 values in green. The spatial correlations between HYCOM and MITgcm LLC4320 maps are indicated in the upper left corners of panels b, e, and h.

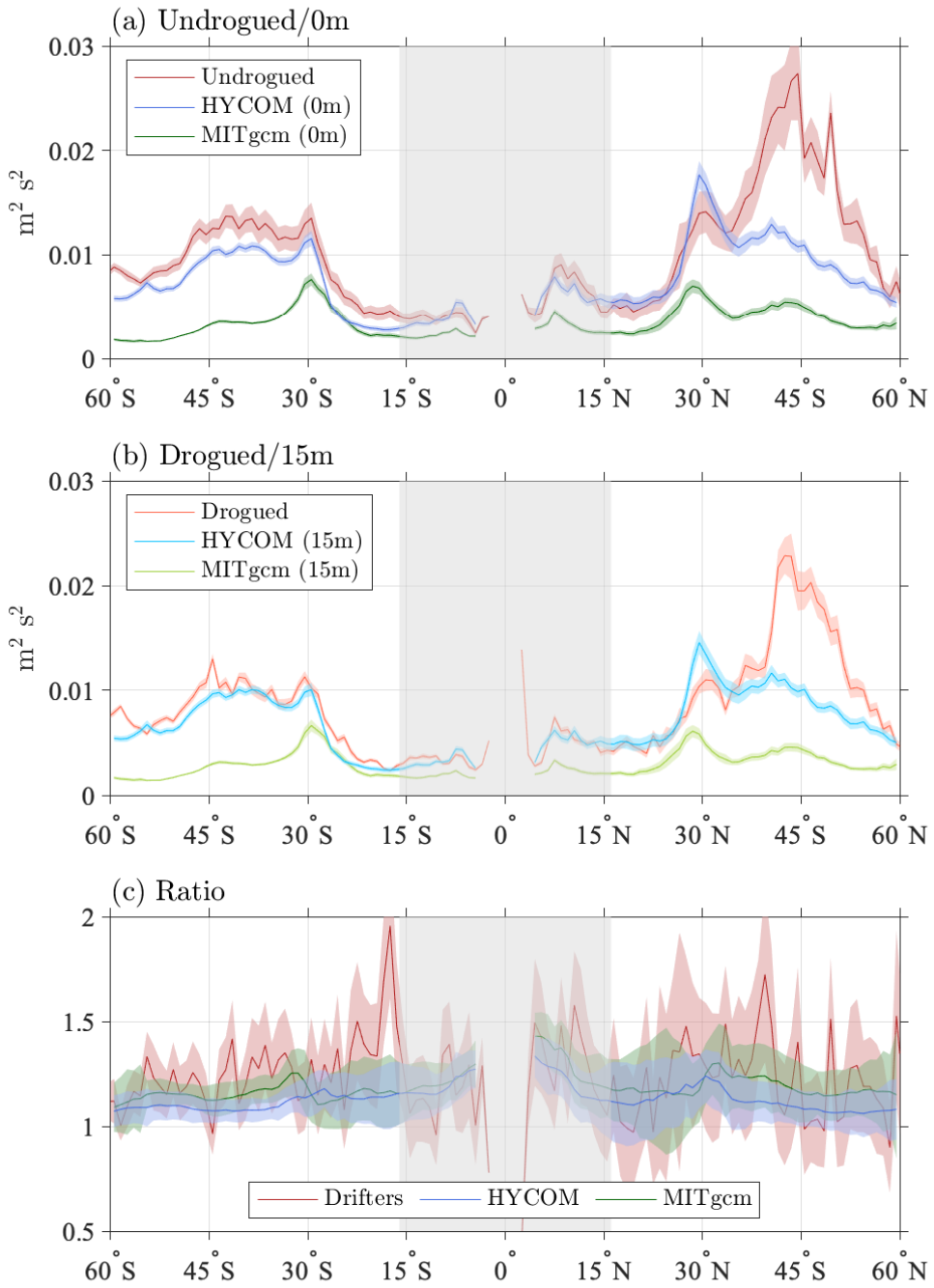


**Figure 6.** Zonally averaged near-inertial ( $\pm[0.9, 1.1]f$ ) KE from (a) undrogued drifters and 0 m model levels, and (b) drogued drifters and 15 m model levels. Ratios of zonal averages of undrogued/drogued drifter KE, and 0 m/15 m model KE, are shown in (c). The gray shaded region in each panel indicates the latitudes where the near-inertial and low-frequency bands exhibit some overlap (see Fig. 1). The shading around each curve corresponds to two standard errors of the calculated  $1^\circ$  zonal averages from the geographical maps.

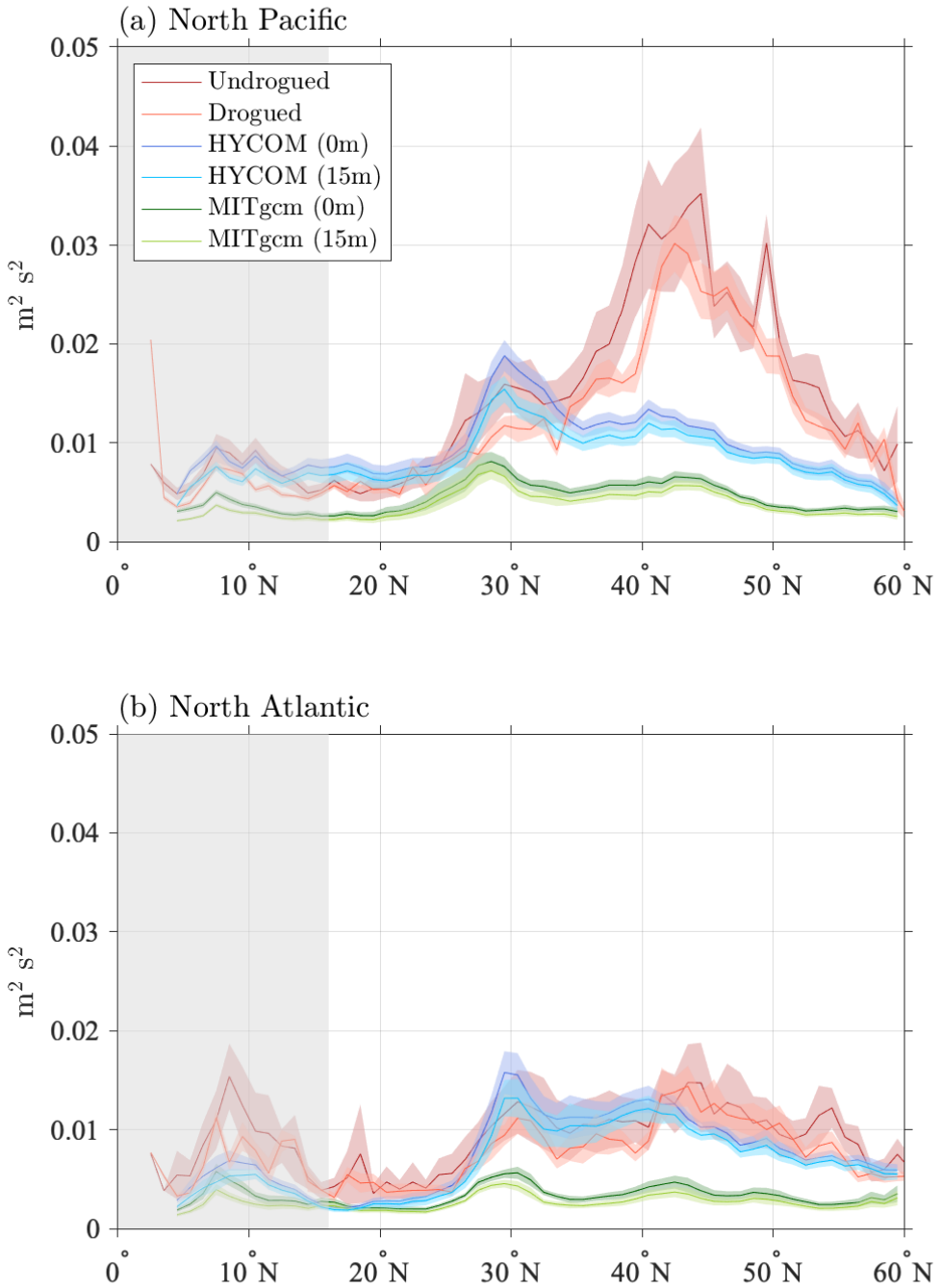


**Figure 7.** Zonally averaged near-inertial KE, as in Fig. 6a and b, but with North Atlantic and North Pacific Ocean basins examined separately. Note that in this figure, both undrogued/0 m and drogued/15 m results are displayed on both subplots.

503            **3.3 Diurnal KE**

504            The most energetic common spatial feature of the diurnal KE maps for the drifters,  
 505 HYCOM, and MITgcm LLC4320 at both depth levels (Figure 8, panels a to f) corre-  
 506 sponds to wind-driven near-inertial motions around  $\pm 30^\circ$  latitude. Another common spa-  
 507 tial feature is a global pattern associated with baroclinic tidal energy constrained equa-  
 508 torward of  $\sim 30^\circ$ . The latter pattern is clearly seen in the models, but is less visible in  
 509 the drifters because of the higher noise level in drifter data. The drifters however seem  
 510 to capture well-known diurnal internal tide hotspots such as in the western north Pa-  
 511 cific. Compared to HYCOM, MITgcm LLC4320 seems to underestimate the wind-driven  
 512 motions, probably because of its less frequent wind forcing (6-hourly compared to 3-hourly).  
 513 In contrast, MITgcm LLC4320 seems to overestimate the tidally-forced diurnal motions,  
 514 probably because of its lack of parameterized topographic wave drag. HYCOM does in-  
 515 clude a wave drag, but the drag is tuned for semi-diurnal tides, not diurnal tides, which  
 516 may as a result be over-damped. Some faint but distinguishable diurnal KE features ex-  
 517 ist at both depth levels along the Agulhas Return Current and the Antarctic Circum-  
 518 polar Current, in both models but not in the drifter maps, perhaps because of the noise  
 519 level and poor sampling. The spatial correlations at both levels between models (0.76  
 520 and 0.75) indicate that the models capture similar KE patterns. At both depth levels,  
 521 the spatial correlations between the drifter results and the model results suggest that  
 522 HYCOM better captures the observations (0.80 and 0.84) than MITgcm LLC4320 does  
 523 (0.61 and 0.69).

524            The KE depth ratio maps for the models (Figure 8, panels h and i) are generally  
 525 similar, allowing us to distinguish wind-driven diurnal motions with low shear around  
 526  $\pm 30^\circ$ , but otherwise exhibit a modest correlation between each other (0.54). The mod-  
 527 els have relatively low correlations with the drifter ratio map (0.19 for HYCOM and 0.21  
 528 for MITgcm LLC4320), likely because of the noisiness of the drifter ratio map.

529            In the model results, we separate the stationary (sometimes referred to as phase-  
 530 locked or coherent) diurnal tidal motions from other diurnal motions using a tidal har-  
 531 monic analysis, here of the two largest constituents ( $K_1$  and  $O_1$ ). Diurnal KE maps ob-  
 532 tained from harmonic analysis, shown in Figure 9 (panels a to d), display enhanced re-  
 533 gions near  $30^\circ$ , but these do not dominate the maps as dramatically as in Figure 8 be-  
 534 cause the wind-driven KE, which is not stationary, is not captured in the harmonic anal-  
 535 ysis. Substantial KE regions are also noticeable equatorward of  $30^\circ$ , especially in the well-  
 536 known diurnal tide hotspot in the western Pacific or along beams of baroclinic motions  
 537 emanating from topographic features (Y. Wang et al., 2021). Except in specific locations  
 538 such as the Sea of Okhotsk, Aleutian Island chain, the Campbell Plateau, and Kergue-  
 539 len Plateau, diurnal KE computed from tidal harmonic analysis drops off steeply pole-  
 540 ward of  $30^\circ$ , the cutoff values separating freely propagating from evanescent diurnal mo-  
 541 tions. For both models, some diurnal KE is captured poleward of  $30^\circ$  by the harmonic  
 542 analysis around some prominent topographic features in the Southern Ocean (for instance  
 543 around the Kerguelen Plateau and the Campbell Plateau) or within the Alaskan Archipelago  
 544 in the North Pacific. These features should correspond to strong barotropic tidal cur-  
 545 rents there, and some evanescent diurnal baroclinic tidal energy, unable to propagate far  
 546 from their generation regions. The features seen in the total diurnal KE model maps within  
 547 the Agulhas Return Current and the Antarctic Circumpolar Current are absent in these  
 548 harmonic analysis maps, suggesting that these are wind-driven in nature.

549            The 0 m to 15 m ratio maps for the diurnal KE from the harmonic analysis (Fig-  
 550 ure 9, panels e and f) are difficult to interpret but appear to be the result of superim-  
 551 posed long-wavelength patterns of barotropic tidal motions and short-wavelet patterns  
 552 of baroclinic tidal motions within the tropical regions, and superimposed patterns of barotropic  
 553 tidal motions and residual wind-driven motions at extratropical latitudes.

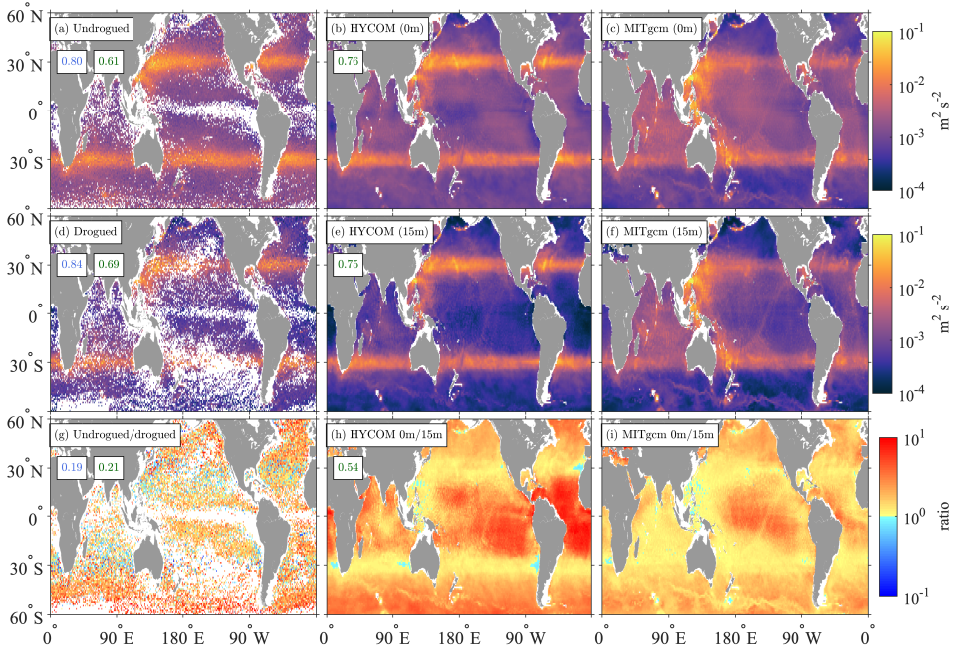


**Figure 8.** Global maps of diurnal ( $\pm[0.9, 1.1]$  cpd) KE from undrogued and drogued drifters (panels a and d), from HYCOM at 0 m and 15 m (panels b and e), and from MITgcm LLC4320 at 0 m and 15 m (panels c and f). The ratios of undrogued to drogued drifter KE, and 0 m to 15 m KE for the HYCOM and MITgcm LLC4320 simulations are shown in panels g, h, and i, respectively. Note the decimal logarithmic color scale for the ratio maps. The spatial correlations between the drifter maps and HYCOM and MITgcm LLC4320 maps are indicated in the upper left corners of panels a, d, and g, with HYCOM values in blue to the left of MITgcm LLC4320 values in green. The spatial correlations between HYCOM and MITgcm LLC4320 maps are indicated in the upper left corners of panels b, e, and h.

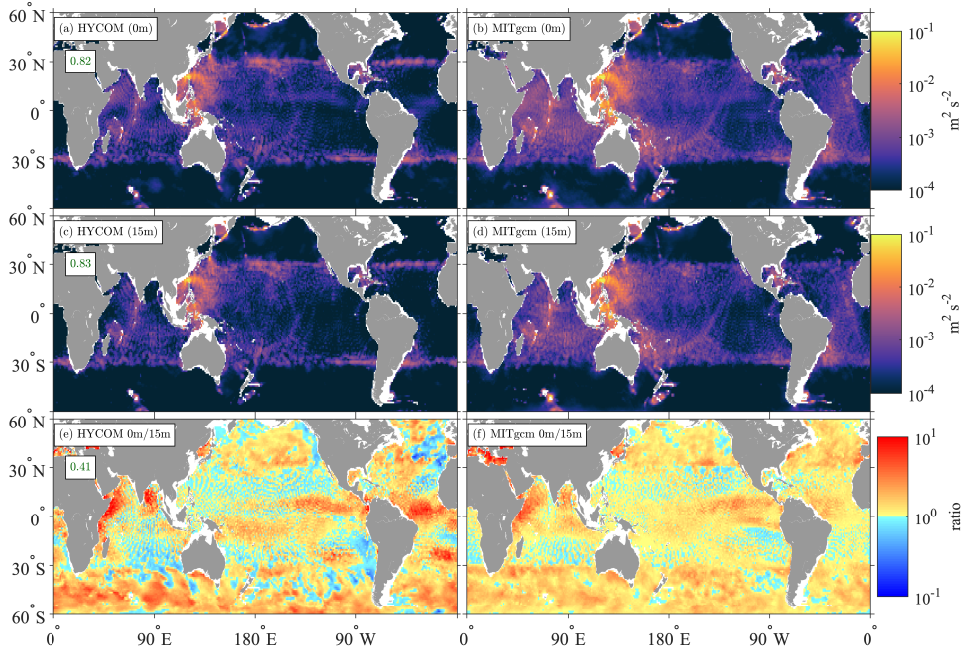


**Figure 9.** Global maps of diurnal KE calculated from harmonic analysis of diurnal tidal constituents  $K_1$  and  $O_1$  for HYCOM at 0 m and 15 m (panels a and c), and from MITgcm LLC4320 at 0 m and 15 m (panels b and d). The ratios of 0 m to 15 m KE for the HYCOM and MITgcm LLC4320 simulations are shown in panels e and f, respectively. Note the decimal logarithmic color scale for the ratio maps. The spatial correlations between HYCOM and MITgcm LLC4320 maps are indicated in the upper left corners of panels a, c, and e.

The spatial correlations of the model diurnal KE maps from the harmonic analysis are slightly higher than for the total diurnal KE maps (0.82 for 0 m and 0.83 for 15 m). In contrast, the spatial correlation between models of the ratio maps is lower (0.41, Figure 9e) than for the total diurnal KE ratio maps (0.54, Figure 8h).

Zonal averages (Figure 10) confirm that HYCOM lies closer to the diurnal peaks in the drifter results near 30°S and 30°N, while MITgcm LLC4320 diurnal energy is too weak in these peak regions. Equatorward of these peaks, MITgcm LLC4320 diurnal energy is generally too strong relative to drifter results, especially near 20°N, the latitude of the northwestern Pacific internal tide hotspot, while HYCOM KE is generally comparable to drifter values. The model diurnal tide harmonic analysis KE values are significantly weaker than the model total diurnal KE values computed from integration of the frequency spectra in the diurnal band. This confirms that the diurnal band consists of other motions (nonstationary diurnal tides, diurnal cycling of Ekman and submesoscale flows, and, in latitudes near 30°, near-inertial flows) as well as stationary diurnal tides.

The ratios of zonally averaged model 0 m KE to zonally averaged model 15 m KE in the diurnal band (Figure 10c) are complicated, as anticipated, and are revealing of model strengths and weaknesses. The ratio of undrogued to drogued drifter diurnal KE is close to two near the equator, and greater than two at high latitudes, with relatively small error bars. The MITgcm LLC4320 total diurnal KE ratio follows the drifter ratio comparatively well over low- and mid-latitudes but is too low at high latitudes. The

574 HYCOM total diurnal KE ratio follows higher latitude drifter values more closely, and  
 575 also follows the mid-latitude drifter ratio well, but is much higher than the drifter ra-  
 576 tio in latitudes equatorward of about  $20^{\circ}$ . Yet, recall that HYCOM tracks the absolute  
 577 drifter KE values equatorward of  $30^{\circ}$  more closely than MITgcm LLC4320 does (pan-  
 578 els a and b). The ratio of 0 m to 15 m diurnal tidal harmonic analysis KE lies relatively  
 579 close to unity over all latitudes, suggesting that stationary diurnal tidal motions are not  
 580 a major contributor to the vertical structure of KE seen in the diurnal band.

### 581 3.4 Semi-diurnal KE

582 Global maps of semi-diurnal kinetic energy (Figure 11, panels a to f) display known  
 583 hotspots of semi-diurnal internal tide motions near, for instance, Hawai'i, the French Poly-  
 584 nesian islands, and the western Pacific. The KE values are substantially higher in the  
 585 simulations, especially MITgcm LLC4320, than in the drifter observations. The hotspots  
 586 are visible in the drifter maps, but less so because of the higher noise level in the drifter  
 587 data. As highlighted in panels b and e, in HYCOM, the semi-diurnal kinetic energy is  
 588 spuriously large in a patch of the high-latitude North Pacific, south of the Aleutians, due  
 589 to a known numerical instability there (Buijsman et al., 2016). As is generally seen in  
 590 other frequency bands, spatial correlations between model KE maps at both 0 and 15  
 591 m are higher (0.82 and 0.83) than the spatial correlations between either model KE map  
 592 and the drifter KE maps, which range between 0.62 and 0.72. Spatial correlations be-  
 593 tween HYCOM and drifter KE maps are slightly higher than spatial correlations between  
 594 MITgcm LLC4320 and drifter KE maps.

595 The ratio maps for the semidiurnal KE band differ substantially from ratio maps  
 596 in other frequency bands. For both models (panels h and i), the ratio values are gener-  
 597 ally close to 1 indicating low differences of KE levels between the surface and 15 m. How-  
 598 ever, the spatial patterns are rather different, resulting in a modest correlation between  
 599 the two model ratio maps (0.44). The ratio map for the drifters is again noisy (panel g),  
 600 yet shows, as in the model maps, values closer to 1 than in other frequency bands. In-  
 601 terestingly, the spatial correlation between the drifter ratio map and the HYCOM ra-  
 602 tio map is about twice as large as for MITgcm LLC4320 (0.13 compared to 0.07). Though  
 603 still admittedly small, this marked difference may be due to the ability of HYCOM to  
 604 represent higher 0 m to 15 m ratio values in the Southern Ocean (and Gulf of Mexico)  
 605 as is seen in the drifter observations.

606 In the zonal averages (Figure 12, panels a and b), as demonstrated by Yu et al. (2019),  
 607 MITgcm LLC4320 KE is higher than drifter KE over all latitudes, by a factor of up to  
 608 four. As indicated in Section 2.2, an overly large tidal forcing, and a lack of the self-attraction  
 609 and loading (SAL) term, in MITgcm LLC4320 artificially enhanced the tidal kinetic en-  
 610 ergy by a factor of about 1.17. This factor is not large enough to explain the discrep-  
 611 ency between MITgcm LLC4320 and drifter observations. Over most latitudes, HYCOM  
 612 lies closer to the drifter KE than MITgcm LLC4320 does. A notable exception to this  
 613 pattern is seen in northern hemisphere high latitudes, where the numerical instability  
 614 in North Pacific HYCOM, mentioned earlier, is exhibited. In addition, the semi-diurnal  
 615 KE in HYCOM is still substantially larger than the drifter KE, in contradistinction to  
 616 the closer agreement seen in comparisons of HYCOM internal tide SSH signatures with  
 617 altimetry (Ansorg et al., 2015; Buijsman et al., 2020). This illustrates the value of com-  
 618 paring models with velocity observations as well as SSH observations.

619 In sharp contrast with results in other frequency bands, the ratios of zonally av-  
 620 eraged undrogued to drogued drifter KE and 0 m to 15 m model KE in the semi-diurnal  
 621 band are consistent with values of unity, to within error bars (Figure 12c), implying that  
 622 there is on average no vertical structure in the semi-diurnal band compared to the other  
 623 bands. However, the large error bars on the drifter and model results may encompass  
 624 the possibility of a small spatially-varying shear.

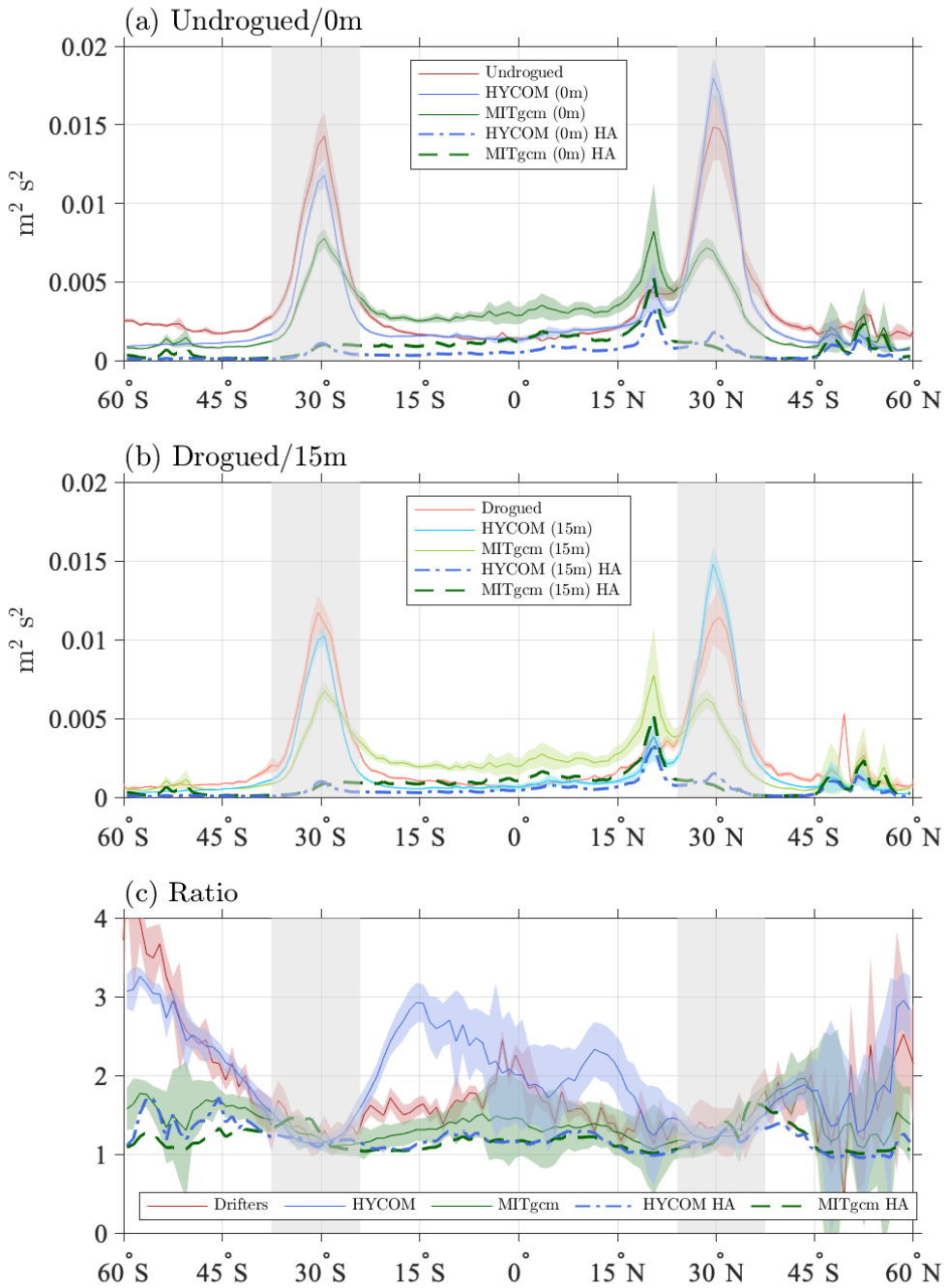


**Figure 10.** Zonally averaged diurnal ( $\pm[0.9, 1.1]$  cpd) KE from (a) undrogued drifters and 0 m model levels, and (b) drogued drifters and 15 m model levels. Ratios of zonal averages of undrogued/drogued drifter KE, and 0 m/15 m model KE, are shown in (c). The zonally averaged diurnal KE from harmonic analysis ("HA", in legend) is also plotted for HYCOM (dash-dotted curve) and MITgcm LLC4320 (dashed curve). The gray shaded region in each panel indicates the latitudes where the diurnal and near-inertial frequency bands overlap (see Fig. 1). The shading around each curve corresponds to two standard errors of the calculated  $1^\circ$  zonal averages from the geographical maps.

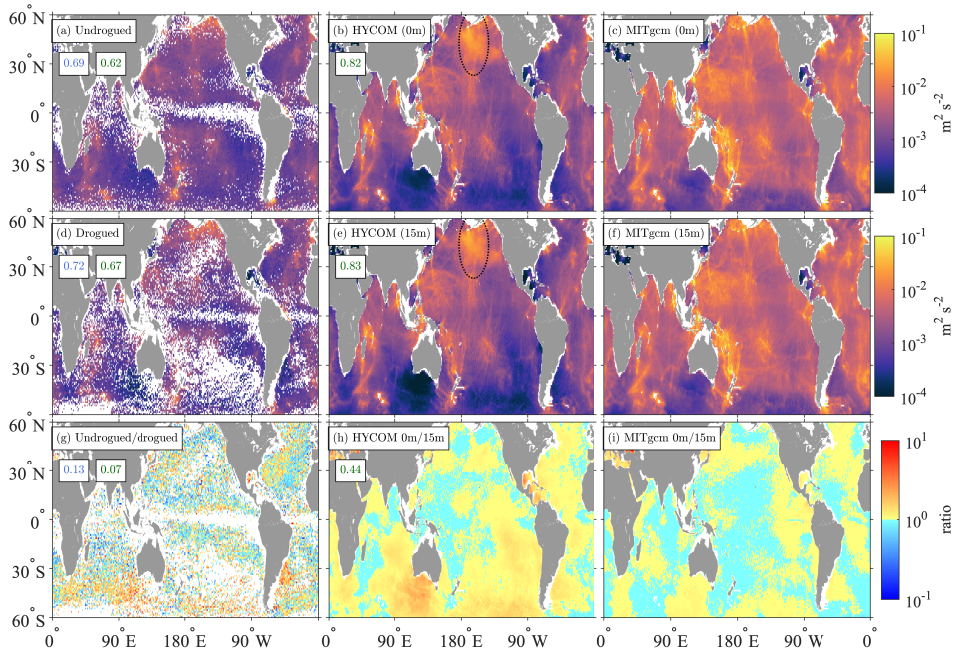


**Figure 11.** Global maps of semi-diurnal ( $\pm[1.9, 2.1]$  cpd) KE from undrogued and drogued drifters (panels a and d), from HYCOM at 0 m and 15 m (panels b and e), and from MITgcm LLC4320 at 0 m and 15 m (panels c and f). The ratios of undrogued to drogued drifter KE, and 0 m to 15 m KE for the HYCOM and MITgcm LLC4320 simulations are shown in panels g, h, and i, respectively. Note the decimal logarithmic color scale for the ratio maps. The spatial correlations between the drifter maps and HYCOM and MITgcm LLC4320 maps are indicated in the upper left corners of panels a, d, and g, with HYCOM values in blue to the left of MITgcm LLC4320 values in green. The spatial correlations between HYCOM and MITgcm LLC4320 maps are indicated in the upper left corners of panels b, e, and h. The North Pacific region of numerical instability in HYCOM (Buijsman et al., 2016) is indicated in panels b and e.

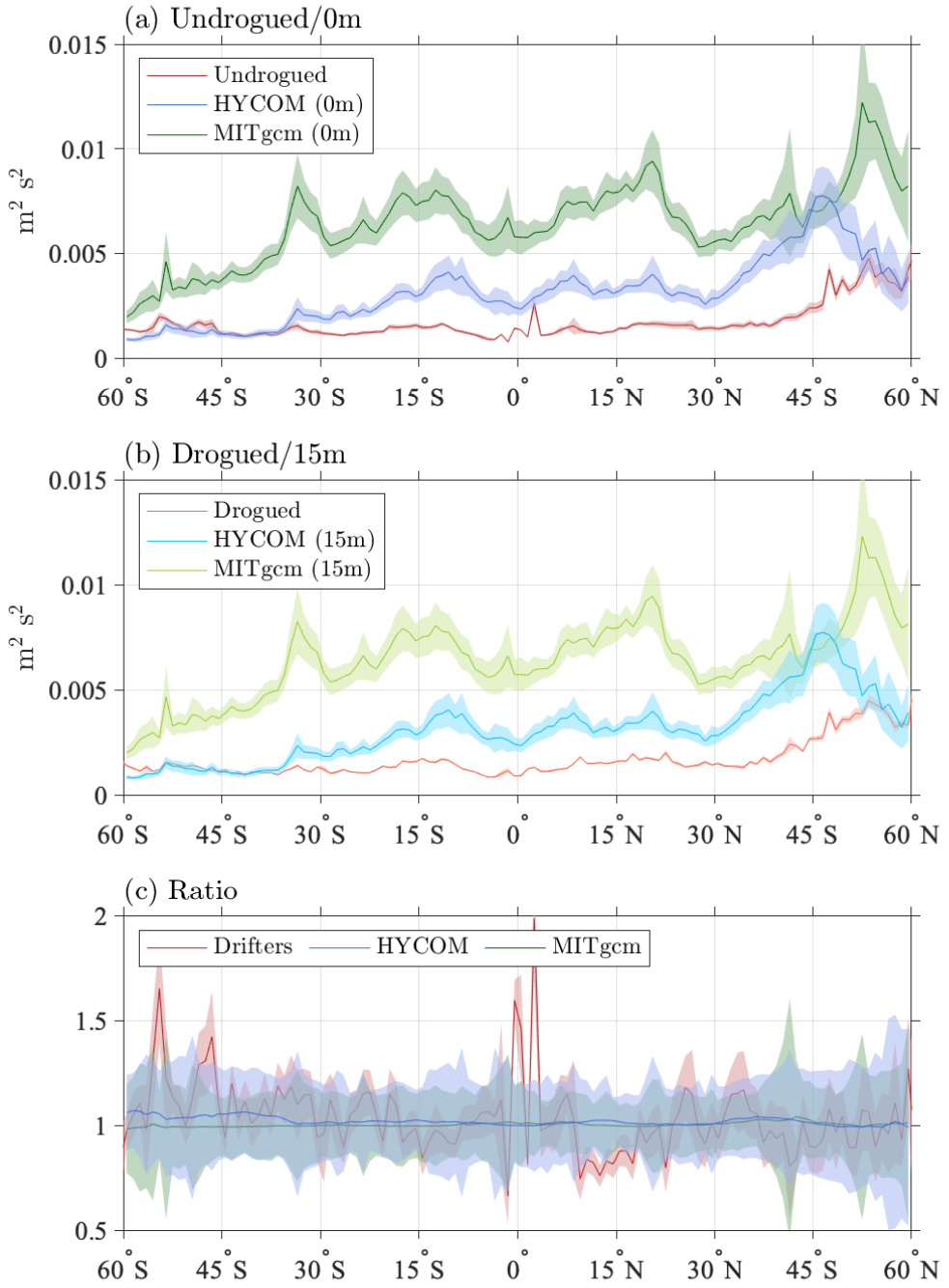


**Figure 12.** Zonally averaged semi-diurnal ( $\pm[1.9, 2.1]$  cpd) KE from (a) undrogued drifters and 0 m model levels, and (b) drogued drifters and 15 m model levels. Ratios of zonal averages of undrogued/drogued drifter KE, and 0 m/15 m model KE, are shown in (c). The shading around each curve corresponds to two standard errors of the calculated  $1^\circ$  zonal averages from the geographical maps.

	Low-frequency	Near-inertial	Diurnal	Semi-diurnal
Mode values				
Drifters	1.35	0.79	1.36	0.80
HYCOM	1.26	1.08	1.22	1.00
MITgcm	1.17	1.16	1.20	1.00
Median values				
Drifters	1.90	1.35	1.86	1.07
HYCOM	1.64	1.12	2.11	1.03
MITgcm	1.36	1.18	1.53	1.00

**Table 1.** Mode and median values of mapped ratios of KE of undrogued to drogued drifters, HYCOM at 0 m to HYCOM at 15 m, and MITgcm LLC4320 at 0 m to 15 m, in four different frequency bands.

Motivated by the “wider and lower” semi-diurnal tidal peaks in drifter spectra compared with model spectra (see insets of Figure 2), we examine in Figure 13 how the model vs. drifter semi-diurnal zonal average comparisons change if the  $\pm[1.9, 2.1]$  cpd semi-diurnal band defined by Yu et al. (2019) is widened to  $\pm[1.6, 2.4]$  cpd in incremental  $\pm0.1$  cpd steps. As the definition of the semi-diurnal band is widened, the drifter KE levels rise gradually, such that, over many latitudes, the agreement between HYCOM and drifters becomes fairly close for the widest definitions of the band (Figure 13, panels c and d). Again, the northern hemisphere high latitudes, where the numerical instability in North Pacific HYCOM is present, represent an exception to this pattern. Over most latitudes, MITgcm LLC4320 KE levels sit well above the drifters—typically by a factor of about two—for all definitions of semi-diurnal band employed in Figure 13. By taking the wider nature of Lagrangian drifter spectra into account, these results suggest that the tidal currents in HYCOM may actually lie closer to the drifter values than the results in Figure 12 indicated. In future work, more direct comparisons of HYCOM and drifters, in which HYCOM is “seeded” with synthetic drifters, are warranted to investigate more comprehensively the biases introduced by the drifter Lagrangian sampling (Zaron & Eliot, 2021). If the closer agreement between HYCOM and drifters holds up under further scrutiny, it would suggest, as in Ansong et al. (2015)’s analysis of internal tide SSH signals, that parameterized topographic wave drag (or some other plausible damping mechanism) is necessary for achieving agreement between semi-diurnal tidal KE in models and observations.

#### 4 Vertical structure: Global averages and discussion

This section provides further discussions of KE vertical structure as diagnosed by ratios of surface (0 m) to 15 m KE. Mode and median values of these ratios, for undrogued to drogued drifters, and for 0 m to 15 m levels in both models, for all frequency bands displayed in our  $1^\circ$  by  $1^\circ$  global maps, are given in Table 1. The global mode and median values are consistent with significant vertical structure, with surface (0 m) values enhanced compared to 15 m values, for the low-frequency, near-inertial, and diurnal bands. The low-frequency and diurnal bands generally display the largest values, followed by the near-inertial band. The semi-diurnal band has the least vertical structure, with most reported values being near one.

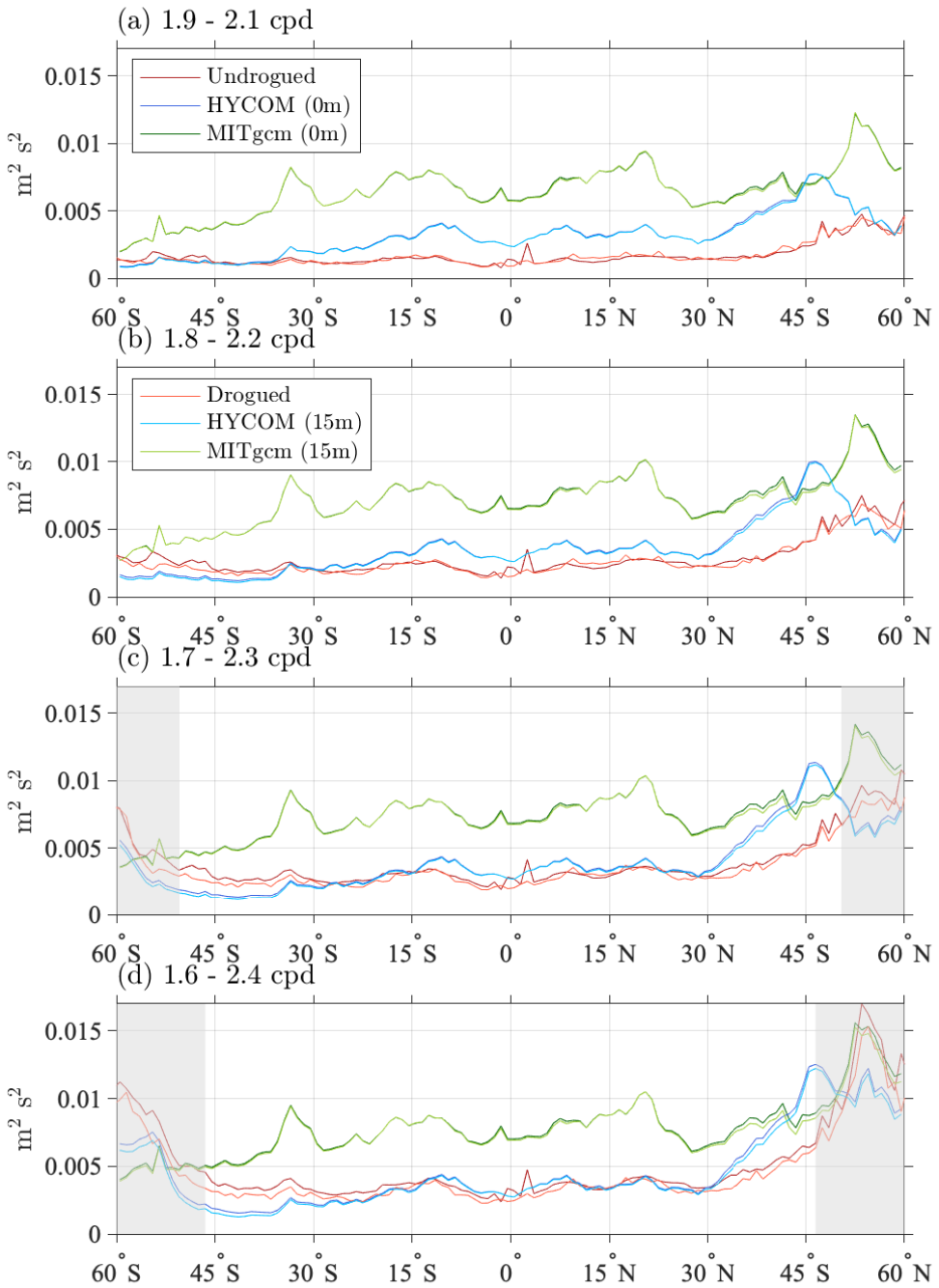


**Figure 13.** Zonally averaged semi-diurnal KE estimates from drifters and model levels calculated by gradually widening the band of frequency integration from  $\pm[1.9, 2.1]$  cpd to  $\pm[1.6, 2.4]$  cpd as indicated in the title of each subplot. Uncertainty estimates are omitted here for clarity. In panels c and d, the gray shaded areas indicate the latitudes where the frequency bands of integration overlap with the near-inertial bands. The legend boxes in panels a and b are applicable to all panels.

If momentum is input at the surface of the ocean, the ratio of surface to near-surface KE will depend on how momentum is mixed downward. In models the downward mixing of momentum is controlled by the vertical mixing scheme employed, in particular, the assumed vertical profile of vertical viscosity. Within the KPP scheme (Large et al., 1994), employed in both HYCOM and MITgcm LLC4320, the vertical viscosity is a cubic profile of depth, yielding increasing viscosity values from a finite surface value, a subsurface maximum, and decreasing values below, down to a background viscosity at the base of a boundary layer. When such a cubic profile is applied to the wind-driven Ekman momentum equation for the surface boundary layer, this results in a frequency-dependent shear which is minimum at the inertial frequency and increases away from the inertial frequency (Elipot, 2006). This theoretical framework is useful to understand how the locally wind-driven component of oceanic currents (Lilly & Elipot, 2021), from the inertial frequency to the low-frequency motions, can be sheared in the upper 15 m of the ocean, as seen here in models and observations. In addition, upper-ocean stratification modulates the ultimate penetration depth of wind momentum (Large & Crawford, 1995; Crawford & Large, 1996; Elipot & Gille, 2009; Dohan & Davis, 2011; Lilly & Elipot, 2021). The reported values of the 0 m to 15 m KE ratio in the drifters and the models are therefore consistent with these expectations.

To aid in interpreting the vertical structure of motions that are not directly wind-driven, such as diurnal tides, semi-diurnal tides, and mesoscale eddies and currents (the latter arising indirectly from wind forcing), it is useful to compute the first three vertical modes (e.g., Gill, 1982; Arbic et al., 2018, among many), for semi-diurnal and diurnal frequencies, as well as for zero frequency (the latter representing the quasi-geostrophic limit). We use five different deep-ocean profiles in a US Navy climatology (Helber et al., 2013), at 10°S, 206°E and at four different latitudes (50°N, 10°N, 6°N, and 50°S) along 210°E. The values of the 0 m to 15 m KE ratio computed from these low vertical modes were greater than one, but only by small amounts (ranging from 1.0001-1.0047), less than the near-inertial values seen in Figure 6c and much less than the low-frequency and total diurnal values seen respectively in Figures 4c and 10c. The low vertical structure ratios in the vertical normal mode analysis are consistent with the lack of vertical structure seen in our semi-diurnal results and diurnal tidal harmonic analysis results, both of which are almost entirely due to tidal motions. We note that semi-diurnal and especially diurnal tidal currents do have a surface-intensified profile (Timko et al., 2013, their Figure 5), but this surface intensification is over vertical scales that are significantly larger than 15 m.

The lack of vertical structure between 0 and 15 m in the low vertical mode analysis is inconsistent with the higher amount of vertical structure seen in our low-frequency and total diurnal results which are likely a superposition of different types of dynamics. Additional physics, such as wind-driven Ekman and other motions, is taking place in the diurnal and low-frequency bands (and in the near-inertial band). The upper-ocean vertical structure in the total diurnal results (Figure 10c) is likely due to non-tidal effects, such as near-inertial flows (in latitudes where they overlap), diurnal cycling in Ekman flows (Price et al., 1986; Price & Sundermeyer, 1999; W.-Y. Sun & Sun, 2020) and submesoscale flows (D. Sun et al., 2020). Regarding the latter possibility, however, we note that the grid spacings in the global models examined here are not sufficient to fully resolve submesoscale eddies (Capet et al., 2008).

The “interior quasi-geostrophic” component (Lapeyre & Klein, 2006) of low-frequency large-scale currents and mesoscale eddies is dominated by barotropic and low baroclinic modes (Wunsch, 1997), or, in an alternative view, by a “surface mode” that is strongest at the surface and approaches zero flow at the seafloor (LaCasce, 2017), due to the influence of bottom topography (LaCasce, 2017) and/or bottom and topographic wave drag (Arbic & Flierl, 2004; Trossman et al., 2017). The surface mode described by LaCasce (2017) decays with depth at the ocean surface, as do the traditional low baroclinic modes.

In addition, low-frequency motions may also have a substantial “surface quasi-geostrophic” component (Lapeyre & Klein, 2006; LaCasce & Wang, 2015), which is surface intensified and may therefore contribute to the weaker motions at 15 m depth relative to the surface. However, the simplest explanation for the vertical structure seen at low-frequencies (Figure 4c) is that it is due to Ekman flows, which exhibit substantial variation over short vertical scales (Elipot & Gille, 2009; Lilly & Elipot, 2021).

A more thorough explanation of the vertical structure in low-frequency, near-inertial, and diurnal flows awaits future work.

## 5 Summary

Near-surface ocean kinetic energy (KE) is an important factor in a variety of problems, including but not limited to air-sea interaction, pollution transport, and satellite mission planning. Such applications require better quantification and understanding of the space-time variability of near-surface oceanic KE, including its frequency dependence and vertical structure (Elipot & Wennegrat, 2021).

In this paper, we have compared KE in undrogued and drogued drifters, which respectively represent flows at the sea surface (0 m) and 15 m depth, to the 0 m and 15 m KE in two different high resolution simulations, MITgcm LLC4320 and HYCOM. The main results employed in the comparisons consist of rotary frequency spectra, and maps and zonal averages made from spatially averaging the rotary spectra over specific frequency bands. We compare both KE levels, at 0 m and 15 m, and the ratio of 0 m to 15 m KE, which we take as a measure of vertical structure. The MITgcm LLC4320 and HYCOM simulations both include tidal forcing alongside atmospheric forcing, implying that the ocean model outputs include high-frequency near-inertial flows, barotropic and baroclinic tides, and an internal gravity wave (IGW) continuum spectrum alongside low-frequency large-scale currents, mesoscale eddies, and Ekman flows. The three-way comparison between drifters and two models allows us to assess the strengths and weaknesses of all three products. The drifters are unable to map the IGW continuum at the highest frequencies, due to a prohibitive noise floor. The drifters can, however, provide global maps of KE in Ekman flows, large-scale currents, mesoscale eddies, near-inertial motions, semi-diurnal tides, and diurnal motions. Diurnal motions include diurnal tides, and diurnal cycling of Ekman and submesoscale flows. In latitudes near 30°, our definitions of diurnal and near-inertial flows overlap, such that near-inertial motions are included in our diurnal results. The stationary component of diurnal tides can be computed separately from other diurnal motions via a tidal harmonic analysis. Maps and zonal averages indicate that stationary diurnal tides are a relatively small component of the KE seen in the diurnal band.

Following Yu et al. (2019), who compared KE in the MITgcm LLC4320 simulation to drifters, we find that near-inertial motions in MITgcm LLC4320 are too weak while semi-diurnal tidal motions are too strong. Here we find that the HYCOM KE values lie closer to the drifters in both the near-inertial and semi-diurnal tidal bands, but for different reasons. In the near-inertial band, HYCOM is stronger than MITgcm LLC4320 due to more frequently updated atmospheric forcing fields. In the semi-diurnal tidal band, HYCOM is weaker than MITgcm LLC4320, due primarily to the parameterized topographic internal wave drag, which simulates the energy lost due to unresolved wave generation and breaking processes, and which is employed in HYCOM but not in MITgcm LLC4320. While HYCOM semi-diurnal tidal KE lies closer to the drifters than MITgcm LLC4320 KE does, the HYCOM semi-diurnal KE is still stronger than the drifter KE if the Yu et al. (2019) definition of semi-diurnal band is employed. However, if we widen the definition of semi-diurnal band from that employed in Yu et al. (2019), the HYCOM tidal KE lies closer to the drifters over most latitudes, while MITgcm LLC4320 semi-diurnal KE is too high. Widening the definition of the semi-diurnal band to accommo-

date comparisons to drifters may be justified, due to the inherently “wider” nature of Lagrangian spectra relative to Eulerian spectra (Zaron & Elipot, 2021). To be more sure of this interpretation, both HYCOM and MITgcm LLC4320 could be seeded with numerical particles and the resulting Lagrangian velocity spectra could be more directly compared to drifter spectra from the actual ocean; this computationally expensive undertaking is left as a topic for future investigation.

Our conclusion that damping parameterizations are necessary for attaining realistic semi-diurnal tidal energy levels is consistent with the results of Ansong et al. (2015), who demonstrated that the sea surface height signature of internal tides in HYCOM is closer to altimetry observations when the HYCOM simulations contain a wave drag than when they do not.

We have shown here that HYCOM also lies closer to drifters than LLC4320 does in the diurnal band, which overlaps with the near-inertial band under the definitions employed here. In addition, we have shown that low-frequency (<0.5 cpd) motions in both models are generally too weak, especially near the equator, that both models suffer from weak near-inertial motions in the northern mid-to-high latitudes, and that numerical instabilities yield overly large tidal HYCOM semidiurnal KE in the North Pacific.

We find that HYCOM generally has higher spatial correlations with drifter observations of KE than MITgcm LLC4320 does, across a wide variety of frequency bands. This result is consistent with Luecke et al. (2020)’s finding that the spatial correlations between HYCOM and mooring observations of KE and temperature variance are higher than the correlations between MITgcm LLC4320 and mooring observations.

We investigate the vertical structure of KE, within all of the frequency bands considered, through global maps, zonal averages, and global mode and median values of a vertical structure ratio, defined as 0 m KE to 15 m KE in the models and undrogued KE to drogued KE in the drifters. With some exceptions noted earlier, in the zonal average results, the models capture the latitude- and frequency- dependence of the vertical structure ratio relatively well. The low-frequency, near-inertial, and diurnal bands display significant vertical structure, while the semi-diurnal band shows little vertical structure. Ekman flows, and their diurnal cycling, likely explain some of the vertical structure seen in the low-frequency and diurnal bands. On a point-by-point basis, the model vs drifter comparisons of the ratios are not as close. The maps of the ratio in the drifters are rather noisy, and spatial correlations between the model ratios and drifter ratios are always less than spatial correlations of the absolute KE between models and drifters.

In ongoing work, we will determine whether the HYCOM and drifter comparison is improved with the employment of data assimilation in operational HYCOM. We will also compare the near-surface KE in coupled high-resolution atmosphere and MITgcm ocean simulations, in which the atmosphere is coupled to the ocean much more frequently than in MITgcm LLC4320, to drifters.

## Acknowledgments

The contributions of J.M.B., D.G., and L.G. to this paper were made while they were undergraduate students.

We thank Roger Samelson for useful comments on vertical structure and the need to quantify model vertical resolution in the upper ocean, Saulo Muller Soares for pointing us towards the Rimac et al. (2013) reference, Bob Helber for providing climatologies for the vertical mode computations described herein, J. Thomas Farrar, Baylor Fox-Kemper, Jeroen Molemaker, and Joe LaCasce for useful discussions on vertical structure and diurnal variations in the mixed layer, Luca Centurioni and Eric D’Asaro for discussions on the equatorial results, and J. Thomas Farrar for discussions on the poten-

809       tial usefulness of the results shown here for S-MODE and satellite velocity-measuring  
 810       missions.

811       B.K.A. gratefully acknowledges funding from US National Science Foundation (NSF)  
 812       grant OCE-1851164 as well as a Research Experience for Undergraduates Supplement  
 813       (for J.M.B.) to that grant; from Office of Naval Research (ONR) grant N00014-18-1-2544;  
 814       and from NASA grants NNX16AH79G, NNX17AH55G, and 80NSSC20K1135. The lat-  
 815       ter NASA grant supported the participation of D.G. and L.G. This research was made  
 816       possible, in part, by the OSiRIS project at University of Michigan and by computing re-  
 817       sources provided by the Advanced Supercomputing Division at NASA. S.E. and E.D.Z.  
 818       gratefully acknowledges funding from US NSF Awards 1851166 and 1850961, respectively.  
 819       A.L.P. and X.Y. are supported by Agence Nationale de la Recherche (ANR). Grant num-  
 820       ber: 17-CE01-0006-01. M.H.A. was supported by Office of Naval Research grant N00014-  
 821       18-1-2404.

822       This paper uses software made available by the Pangeo project, by jLab (Lilly, 2021)  
 823       and by the “cmocean” package (Thyng et al., 2016). MITgcm LLC4320 output is avail-  
 824       able at [https://data.nas.nasa.gov/ecco/data.php?dir=/eccodata/l1c\\_4320](https://data.nas.nasa.gov/ecco/data.php?dir=/eccodata/l1c_4320). The  
 825       surface drifter data are available at [https://www.aoml.noaa.gov/phod/gdp/hourly\\_data.ph](https://www.aoml.noaa.gov/phod/gdp/hourly_data.ph). HYCOM output can be accessed via the OSiRIS infrastructure. Co-authors B.K.A.  
 826       and J.F.S. can be contacted for details on OSiRIS access. The Matlab code used to pro-  
 827       cess the MITgcm LLC4320 and HYCOM outputs into the results used in this paper, the  
 828       results from MITgcm 4320, HYCOM, and processed drifter data, and the code used to  
 829       produce all of the plots in the paper, are provided in Arbic et al. (2022); see also <https://tinyurl.com/2p9eh5yp> (a permanent DOI <https://doi.org/10.7302/PTG7-YW20> is  
 830       pending).

## 833       References

- 834       Alford, M. H. (2003a). Redistribution of energy available for ocean mixing by long-  
 835       range propagation of internal waves. *Nature*, 423, 159–162. doi: 10.1038/  
 836       nature01628
- 837       Alford, M. H. (2003b). Improved global maps and 54-year history of wind-work on  
 838       ocean inertial motions. *Geophysical Research Letters*, 30, 1424. doi: 10.1029/  
 839       2002GL016614
- 840       Ansong, J. K., Arbic, B. K., Buijsman, M. C., Richman, J. G., Shriver, J. F., &  
 841       Wallcraft, A. J. (2015). Indirect evidence for substantial damping of low-mode  
 842       internal tides in the open ocean. *Journal of Geophysical Research: Oceans*,  
 843       120(9), 6057–6071. doi: 10.1002/2015JC010998
- 844       Arbic, B. K., Alford, M., Ansong, J., Buijsman, M., Ciotti, R., Farrar, J., ... Zhao,  
 845       Z. (2018). A primer on global internal tide and internal gravity wave con-  
 846       tinuum modeling in HYCOM and MITgcm. In E. Chassignet, A. Pascual,  
 847       J. Tintoré, & J. Verron (Eds.), *New frontiers in operational oceanography* (pp.  
 848       307–392). GODAE Ocean View. doi: 10.17125/gov2018.ch13
- 849       Arbic, B. K., Eliot, S., Menemenlis, D., & Shriver, J. F. (2022). *Frequency de-  
 850       pendence and vertical structure of ocean surface kinetic energy from global  
 851       high-resolution models and surface drifter observations [Data set]*. University of  
 852       Michigan–Deep Blue Data. Retrieved from <https://tinyurl.com/2p9eh5yp>  
 853       doi: <https://doi.org/10.7302/PTG7-YW20>
- 854       Arbic, B. K., & Flierl, G. R. (2004). Baroclinically unstable geostrophic turbu-  
 855       lence in the limits of strong and weak bottom Ekman friction: Application to  
 856       Midocean Eddies. *Journal of Physical Oceanography*, 34, 2257–2273. doi:  
 857       10.1175/1520-0485(2004)034<2257:BUGTIT>2.0.CO;2
- 858       Arbic, B. K., Richman, J. G., Shriver, J. F., Timko, P. G., Metzger, E. J., &  
 859       Wallcraf, A. J. (2012). Global modeling of internal tides within an ed-  
 860       dying ocean general circulation model. *Oceanography*, 25, 20–29. doi:

- 861 10.5670/oceanog.2012.38
- 862 Arbic, B. K., Wallcraft, A. J., & Metzger, E. J. (2010). Concurrent simulation of  
863 the eddying general circulation and tides in a global ocean model. *Ocean Mod-  
864 elling*, 32(3), 175–187. doi: 10.1016/j.ocemod.2010.01.007
- 865 Ardhuin, F., Brandt, P., Gaultier, L., Donlon, C., Battaglia, A., Boy, F., ... Stam-  
866 mer, D. (2019). SKIM, a candidate satellite mission exploring global  
867 ocean currents and waves. *Frontiers in Marine Science*, 6, 209. doi:  
868 10.3389/fmars.2019.00209
- 869 Bleck, R. (2002). An oceanic general circulation model framed in hybrid  
870 isopycnic-Cartesian coordinates. *Ocean Modelling*, 4, 55–88. doi: 10.1016/  
871 S1463-5003(01)00012-9
- 872 Buijsman, M. C., Ansong, J. K., Arbic, B. K., Richman, J. G., Shriver, J. F., Timko,  
873 P. G., ... Zhao, Z. (2016). Impact of parameterized internal wave drag on  
874 the semidiurnal energy balance in a global ocean circulation model. *Journal of  
875 Physical Oceanography*, 46, 1399–1419. doi: 10.1175/JPO-D-15-0074.1
- 876 Buijsman, M. C., Arbic, B. K., Richman, J. G., Shriver, J. F., Wallcraft, A. J., &  
877 Zamudio, L. (2017). Semidiurnal internal tide incoherence in the equato-  
878 rial Pacific. *Journal of Geophysical Research Oceans*, 122, 5286–5305. doi:  
879 10.1002/2016JC012590
- 880 Buijsman, M. C., Stephenson, G. R., Ansong, J. K., Arbic, B. K., Green, J. A. M.,  
881 Richman, J. G., ... Zhao, Z. (2020). On the interplay between horizon-  
882 tal resolution and wave drag and their effect on tidal baroclinic mode waves  
883 in realistic global ocean simulations. *Ocean Modelling*, 152, 101656. doi:  
884 10.1016/j.ocemod.2020.101656
- 885 Capet, X., McWilliams, J. C., Molemaker, M. J., & Shchepetkin, A. F. (2008).  
886 Mesoscale to submesoscale transition in the California Current System. Part  
887 III: Energy balance and flux. *Journal of Physical Oceanography*, 38, 2256–  
888 2269. doi: 10.1175/2008JPO3810.1
- 889 Chaigneau, A., Pizarro, O., & Rojas, W. (2008). Global climatology of near-inertial  
890 current characteristics from Lagrangian observations. *Geophysical Research  
891 Letters*, 35(13), L13603. doi: 10.1029/2008GL034060
- 892 Chassignet, E. P., Hurlburt, H. E., Metzger, E. J., Smedstad, O. M., Cummings,  
893 J. A., Halliwell, G. R., ... Wilkin, J. (2009). Global ocean prediction with  
894 the HYbrid Coordinate Ocean Model (HYCOM). *Oceanography*, 22. doi:  
895 10.5670/oceanog.2009.39
- 896 Chereskin, T. K., Rocha, C., Gille, S. T., Menemenlis, D., & Passaro, M. (2019).  
897 Characterizing the transition from balanced to unbalanced motions in the  
898 Southern California current. *Journal of Geophysical Research Oceans*, 124,  
899 2088–2109. doi: 10.1029/2018jc014583
- 900 Crawford, G. B., & Large, W. G. (1996). A numerical investigation of resonant in-  
901 ertrial response of the ocean to wind forcing. *Journal of Physical Oceanography*,  
902 26, 873–891. doi: 10.1175/1520-0485(1996)026<0873:ANIORI>2.0.CO;2
- 903 Cronin, M. F., & Coauthors. (2019). Air-sea fluxes with a focus on heat and momen-  
904 tum. *Frontiers in Marine Science*, 6. doi: 10.3389/fmars.2019.00430
- 905 Dohan, K., & Davis, R. E. (2011). Mixing in the transition layer during  
906 two storm events. *Journal of Physical Oceanography*, 41, 42–66. doi:  
907 10.1175/2010JPO4253.1
- 908 Egbert, G. D., Bennett, A. F., & Foreman, M. G. G. (1994). TOPEX/POSEIDON  
909 tides estimated using a global inverse model. *Journal of Geophysical Research*,  
910 99, 24821–24852. doi: 10.1029/94JC01894
- 911 Egbert, G. D., & Erofeeva, S. Y. (2002). Efficient inverse modeling of barotropic  
912 ocean tides. *Journal of Atmospheric and Oceanic Technology*, 19, 183–204.  
913 doi: 10.1175/1520-0426(2002)019<0183:EIMOB>2.0.CO;2
- 914 Eliot, S. (2006). *Spectral characterization of Ekman velocities in the Southern  
915 Ocean based on surface drifter trajectories* (Unpublished doctoral dissertation).

- 916 Scripps Institution of Oceanography, University of California, San Diego.
- 917 Elipot, S., & Gille, S. T. (2009). Ekman layers in the Southern Ocean: spectral  
918 models and observations, vertical viscosity and boundary layer depth. *Ocean  
919 Science*, 5, 115–139. doi: 10.5194/os-5-115-2009
- 920 Elipot, S., & Lumpkin, R. (2008). Spectral description of oceanic near-surface vari-  
921 ability. *Geophysical Research Letters*, 35(5). doi: 10.1029/2007GL032874
- 922 Elipot, S., Lumpkin, R., Perez, R. C., Lilly, J. M., Early, J. J., & Sykulski, A. M.  
923 (2016). A global surface drifter data set at hourly resolution. *Journal of Geo-  
924 physical Research: Oceans*, 121(5), 2937-2966. doi: 10.1002/2016JC011716
- 925 Elipot, S., Lumpkin, R., & Prieto, G. (2010). Modification of inertial oscillations by  
926 the mesoscale eddy field. *Journal of Geophysical Research: Oceans*, 115(C9).  
927 doi: 10.1029/2009JC005679
- 928 Elipot, S., & Wennegrat, J. O. (2021). Vertical structure of near-surface currents:  
929 Importance, state of knowledge, and measurement challenges. *CLIVAR Vari-  
930 tions*, 19. doi: 10.5065/ybca-0s03
- 931 Ferrari, R., & Wunsch, C. (2009). Ocean circulation kinetic energy: Reservoirs,  
932 sources and sinks. *Annual Review of Fluid Mechanics*, 41(1), 253-282. doi: 10  
933 .1146/annurev.fluid.40.111406.102139
- 934 Flexas, M. M., Thompson, A. F., Torres, H. S., Klein, P. J., Farrar, J. T., Zhang,  
935 H., & Menemenlis, D. (2019). Global estimates of the energy transfer from  
936 the wind to the ocean, with emphasis on near-inertial oscillations. *Journal of  
937 Geophysical Research Oceans*, 124, 5723–5746. doi: 10.1029/2018JC014453
- 938 Furuichi, N., Hibiya, T., & Niwa, Y. (2008). Model-predicted distribution of wind-  
939 induced internal wave energy in the world's oceans. *Journal of Geophysical Re-  
940 search*, 113, C09034. doi: 10.1029/2008JC004768
- 941 Garrett, C., & Munk, W. (1975). Space-time scales of internal waves: A progress re-  
942 port. *Journal of Geophysical Research (1896-1977)*, 80(3), 291–297. doi: 10  
943 .1029/JC080i003p00291
- 944 Gill, A. E. (1982). *Atmosphere-Ocean Dynamics*. Academic Press.
- 945 Gonella, J. (1972). A rotary-component method for analysing meteorological and  
946 oceanographic vector time series. *Deep-Sea Research*, 19, 833–846. doi: 10  
947 .1016/0011-7471(72)90002-2
- 948 Helber, R. W., Townsend, T. L., Barron, C. N., Dastugue, J. M., & Carnes, M. R.  
949 (2013). *Validation test report for the Improved Synthetic Ocean Profile (ISOP)  
950 System, Part 1: Synthetic profile methods and algorithm* (Tech. Rep.). NRL  
951 Report NRL/MR/7320 13-9364.
- 952 Hendershott, M. C. (1972). The effects of solid earth deformation on global ocean  
953 tides. *Geophysical Journal International*, 29, 389–402. doi: 10.1111/j.1365  
954 -246X.1972.tb06167.x
- 955 Hogan, T. F., Liu, M., Ridout, J. A., Peng, M. S., Whitcomb, T. R., Ruston, B. C.,  
956 ... Chang, S. W. (2014). The Navy Global Environmental Model. *Oceanogra-  
957 phy*, 27, 116–125. doi: 10.5670/oceanog.2014.73
- 958 Jayne, S. R., & St. Laurent, L. C. (2001). Parameterizing tidal dissipation over  
959 rough topography. *Geophysical Research Letters*, 28, 811–814. doi: 10.1029/  
960 2000GL012044
- 961 Kerry, C. G., Powell, B. S., & Carter, G. S. (2016). Quantifying the incoherent  
962  $M_2$  internal tide in the Philippine Sea. *Journal of Physical Oceanography*, 46,  
963 2483–2491. doi: 10.1175/JPO-D-16-0023.1
- 964 Kodaira, T., Thompson, K. R., & Bernier, N. B. (2015). Prediction of  $M_2$  tidal sur-  
965 face currents by a global baroclinic ocean model and evaluation using observed  
966 drifter trajectories. *Journal of Geophysical Research Oceans*, 121, 6159–6183.  
967 doi: 10.1002/2015JC011549
- 968 LaCasce, J. H. (2017). The prevalence of oceanic surface modes. *Geophysical Re-  
969 search Letters*, 44, 11097–11105. doi: 10.1002/2017GL075430
- 970 LaCasce, J. H., & Wang, J. (2015). Estimating subsurface velocities from surface

- 971 fields with idealized stratification. *Journal of Physical Oceanography*, 45,  
 972 2424–2435. doi: 10.1175/JPO-D-14-0206.1
- 973 Lapeyre, G., & Klein, P. (2006). Dynamics of the upper oceanic layers in terms  
 974 of surface quasigeostrophy theory. *Journal of Physical Oceanography*, 36, 165–  
 975 176. doi: 10.1175/JPO2840.1
- 976 Large, W. G., & Crawford, G. B. (1995). Observations and simulations of  
 977 upper-ocean response to wind events during the Ocean Storms Experiment.  
 978 *Journal of Physical Oceanography*, 25, 2831–2852. doi: 10.1175/1520-0485(1995)025<2831:OASOUO>2.0.CO;2
- 980 Large, W. G., McWilliams, J. C., & Doney, S. C. (1994). Oceanic vertical mixing: A  
 981 review and a model with a nonlocal boundary layer parameterization. *Journal  
 982 of Geophysical Research*, 32, 363–403. doi: 10.1029/94RG01872
- 983 Le Boyer, A., & Alford, M. H. (2020). Variability and sources of the internal wave  
 984 continuum examined from global moored velocity records. *Journal of Physical  
 985 Oceanography*, in review, 1–20.
- 986 Lévy, M., Franks, P. J., & Smith, K. S. (2018). The role of submesoscale currents  
 987 in structuring marine ecosystems. *Nature Communications*, 9. doi: 10.1038/  
 988 s41467-018-07059-3
- 989 Lilly, J. M. (2021). *jLab: A data analysis package for Matlab, v.1.7.0 [Data set]*.  
 990 Zenodo. doi: 10.5281/zenodo.4547006
- 991 Lilly, J. M., & Elipot, S. (2021). A unifying perspective on transfer function solu-  
 992 tions to the unsteady Ekman problem. *Fluids*, 6(2). Retrieved from <https://www.mdpi.com/2311-5521/6/2/85> doi: 10.3390/fluids6020085
- 993 Luecke, C. A., Arbic, B. K., Richman, J. G., Shriner, J. F., Alford, M. H., Ansong,  
 994 J. K., ... Zamudio, L. (2020). Statistical comparisons of temperature vari-  
 995 ance and kinetic energy in global ocean models and observations: Results  
 996 from mesoscale to internal wave frequencies. *Journal of Geophysical Research  
 997 Oceans*, 125, e2019JC015306. doi: 10.1029/2019JC015306
- 998 Lumpkin, R., & Johnson, G. C. (2013). Global ocean surface velocities from  
 999 drifters: Mean, variance, El Niño–Southern Oscillation response, and sea-  
 1000 sonal cycle. *Journal of Geophysical Research: Oceans*, 118(6), 2992–3006. doi:  
 1002/10.1002/jgrc.20210
- 1003 Lumpkin, R., & Pazos, M. (2007). Measuring surface currents with surface velocity  
 1004 program drifters: the instrument, its data and some recent results. *Lagrangian  
 1005 analysis and prediction of coastal and ocean dynamics*, 2, 39.
- 1006 Lumpkin, R., Özgökmen, T., & Centurioni, L. (2017). Advances in the application  
 1007 of surface drifters. *Annual Review of Marine Science*, 9(1), 59–81. doi: 10  
 10.1146/annurev-marine-010816-060641
- 1008 Marshall, J., Adcroft, A., Hill, C., Perelman, L., & Heisey, C. (1997). A finite-  
 1009 volume, incompressible Navier Stokes model for studies of the ocean on parallel  
 1010 computers. *Journal of Geophysical Research Oceans*, 102 (C3), 5753–5766. doi:  
 1012 10.1029/96JC02775
- 1013 Maximenko, N., Niiler, P., Rio, M.-H., Melnichenko, O., Centurioni, L., Cham-  
 1014 bers, D., ... Galperin, B. (2009). Mean dynamic topography of the ocean  
 1015 derived from satellite and drifting buoy data using three different tech-  
 1016 niques. *Journal of Atmospheric and Oceanic Technology*, 26, 1910–1919.  
 1017 doi: 10.1175/2009JTECHO672.1
- 1018 Mooers, C. N. (1973). A technique for the cross spectrum analysis of pairs of  
 1019 complex-valued time series, with emphasis on properties of polarized com-  
 1020 ponents and rotational invariants. *Deep-Sea Research*, 20, 1129–1141. doi:  
 1021 10.1016/0011-7471(73)90027-2
- 1022 Morrow, R., Fu, L.-L., Arduin, F., Benkiran, M., Chapron, B., Cosme, E., ...  
 1023 Zaron, E. D. (2019). Global observations of fine-scale ocean surface topography  
 1024 with the Surface Water and Ocean Topography (SWOT) mission. *Frontiers in  
 1025 Marine Science*, 6, 232. doi: 10.3389/fmars.2019.00232

- 1026 Müller, M., Arbic, B. K., Richman, J. G., Shriner, J. F., Kunze, E. L., Scott, R. B.,  
 1027 ... Zamudio, L. (2015). Toward an internal gravity wave spectrum in  
 1028 global ocean models. *Geophysical Research Letters*, *42*, 3474–3481. doi:  
 1029 10.1002/2015GL063365
- 1030 Müller, M., Cherniawsky, J. Y., Foreman, M. G. G., & von Storch, J.-S. (2012).  
 1031 Global  $M_2$  internal tide and its seasonal variability from high resolution ocean  
 1032 circulation and tide modeling. *Geophysical Research Letters*, *39*(19). doi:  
 1033 10.1029/2012GL053320
- 1034 Nelson, A. D., Arbic, B. K., Mememenlis, D., Peltier, W. R., Grisouard, N., & Kly-  
 1035 mak, J. M. (2020). Improved internal wave spectral continuum in a regional  
 1036 ocean model. *Journal of Geophysical Research Oceans*, *125*, e2019JC015974.  
 1037 doi: 10.1029/2019JC015974
- 1038 Nelson, A. D., Arbic, B. K., Zaron, E. D., Savage, A. C., Richman, J. G., & Buijs-  
 1039 man, J. F., M. C. Shriner. (2019). Toward realistic nonstationarity of semidiurnal  
 1040 baroclinic tides in a hydrodynamic model. *Journal of Geophysical Research  
 1041 Oceans*, *124*, 6632–6642. doi: 10.1029/2018JC014737
- 1042 Ngodock, H. E., Souopgui, I., Wallcraft, A. J., Richman, J. G., Shriner, J., Jay F.,  
 1043 & Arbic, B. K. (2016). On improving the accuracy of the  $M_2$  barotropic  
 1044 tides embedded in a high-resolution global ocean circulation model. *Ocean  
 1045 Modelling*, *97*, 16–26. doi: 10.1016/j.ocemod.2015.10.011
- 1046 Niiler, P. P., & Paduan, J. D. (1995). Wind-driven motions in the Northeast Pacific  
 1047 as measured by Lagrangian drifters. *Journal of Physical Oceanography*, *25*(11),  
 1048 2819–2830. doi: 10.1175/1520-0485(1995)025<2819:WDMITN>2.0.CO;2
- 1049 Olascoaga, M. J., Beron-Vera, F. J., Miron, P., Triñanes, J., Putman, N. F., Lump-  
 1050 kin, R., & Goni, G. J. (2020). Observation and quantification of inertial effects  
 1051 on the drift of floating objects at the ocean surface. *Physics of Fluids*, *32*. doi:  
 1052 10.1063/1.5139045
- 1053 Pan, Y., Arbic, B. K., Nelson, A. D., Menemenlis, D., Peltier, W. R., Xu, W., & Li,  
 1054 Y. (2020). Numerical investigation of mechanisms underlying oceanic internal  
 1055 gravity wave power-law spectra. *Journal of Physical Oceanography*, *50*. doi:  
 1056 10.1175/JPO-D-20-0039.1
- 1057 Pollard, R. T., & Millard, R. C. (1970). Comparison between observed and simu-  
 1058 lated wind-generated inertial oscillations. *Deep-Sea Research*, *17*, 813–821. doi:  
 1059 10.1016/0011-7471(70)90043-4
- 1060 Polton, J. A., Lewis, D. M., & Belcher, S. E. (2005). The role of wave-induced  
 1061 Coriolis–Stokes forcing on the wind-driven mixed layer. *Journal of Physical  
 1062 Oceanography*, *35*(4), 444–457. doi: <https://doi.org/10.1175/JPO2701.1>
- 1063 Ponte, A. L., & Klein, P. (2015). Incoherent signature of internal tides on sea  
 1064 level in idealized numerical simulations. *Geophysical Research Letters*, *42*,  
 1065 1520–1526. doi: 10.1002/2014GL062583
- 1066 Poulain, P.-M., & Centurioni, L. (2015). Direct measurements of World Ocean  
 1067 tidal currents with surface drifters. *Journal of Geophysical Research: Oceans*,  
 1068 *120*(10), 6986–7003. doi: 10.1002/2015JC010818
- 1069 Price, J. F., & Sundermeyer, M. A. (1999). Stratified Ekman layers. *Journal of Geo-  
 1070 physical Research*, *104*, 20467–20494. doi: 10.1029/1999JC900164
- 1071 Price, J. F., Weller, W. A., & Pinkel, R. (1986). Diurnal cycling: Observa-  
 1072 tions and models of the upper ocean response to diurnal heating, cooling  
 1073 and wind mixing. *Journal of Geophysical Research*, *91*, 8411–8427. doi:  
 1074 10.1029/JC091iC07p08411
- 1075 Qiu, B., Chen, S., Klein, P., Wang, J., Torres, H., & Fu, L.-L. (2018). Sea-  
 1076 sonality in transition scale from balanced to unbalanced motions in the  
 1077 world ocean. *Journal of Physical Oceanography*, *48*, 591–605. doi:  
 1078 10.1175/JPO-D-17-0169.1
- 1079 Ray, R. D. (1998). Ocean self-attraction and loading in numerical tidal models. *Ma-  
 1080 rine Geodesy*, *21*, 181–192. doi: 10.1080/01490419809388134

- 1081 Ray, R. D., & Zaron, E. D. (2011). Non-stationary internal tides observed with  
 1082 satellite altimetry. *Geophysical Research Letters*, 38, L17609. doi: 10.1029/  
 1083 2011GL048617
- 1084 Richman, J. G., Arbic, B. K., Shriver, J. F., Metzger, E. J., & Wallcraft, A. J.  
 1085 (2012). Inferring dynamics from the wavenumber spectra of an eddying global  
 1086 ocean model with embedded tides. *Journal of Geophysical Research: Oceans*,  
 1087 117(C12). doi: 10.1029/2012JC008364
- 1088 Rimac, A., von Storch, J.-S., Eden, C., & Haak, H. (2013). The influence of high-  
 1089 resolution wind stress field on the power input to near-inertial motions in the  
 1090 ocean. *Geophysical Research Letters*, 40, 4882–4886. doi: 10.1002/grl.50929
- 1091 Rocha, C. B., Chereskin, T. K., Gille, S. T., & Menemenlis, D. (2016). Mesoscale  
 1092 to submesoscale wavenumber spectra in Drake Passage. *Journal of Physical*  
 1093 *Oceanography*, 46(2), 601–620. doi: 10.1175/JPO-D-15-0087.1
- 1094 Rocha, C. B., Gille, S. T., Chereskin, T. K., & Menemenlis, D. (2016). Seasonal-  
 1095 ity of submesoscale dynamics in the Kuroshio Extension. *Geophysical Research*  
 1096 *Letters*, 43(21), 11,304–311,311. doi: 10.1002/2016GL071349
- 1097 Rodriguez, E., Wineteer, A., Perkovic-Martin, D., Gal, T., Anderson, S., Zuckerman,  
 1098 S., ... Yang, X. (2020). Ka-Band Doppler scatterometry over a Loop Current  
 1099 eddy. *Remote Sensing*, 12, 2388. doi: 10.3390/rs12152388
- 1100 Savage, A. C., Arbic, B. K., Alford, M. H., Ansong, J. K., Farrar, J. T., Menemenlis,  
 1101 D., ... Zamudio, L. (2017b). Spectral decomposition of internal gravity wave  
 1102 sea surface height in global models. *Journal of Geophysical Research: Oceans*,  
 1103 122(10), 7803–7821. doi: 10.1002/2017JC013009
- 1104 Savage, A. C., Arbic, B. K., Richman, J. G., Shriver, J. F., Alford, M. H., Buijsman,  
 1105 M. C., ... Zamudio, L. (2017a). Frequency content of sea surface height vari-  
 1106 ability from internal gravity waves to mesoscale eddies. *Journal of Geophysical*  
 1107 *Research: Oceans*, 122(3), 2519–2538. doi: 10.1002/2016JC012331
- 1108 Shriver, J. F., Richman, J. G., & Arbic, B. K. (2014). How stationary are the inter-  
 1109 nals tides in a high-resolution global ocean circulation model? *Journal of Geo-  
 1110 physical Research Oceans*, 119, 2769–2787. doi: 10.1002/2013JC009423
- 1111 Simmons, H. L., & Alford, M. H. (2012). Simulating the long-range swell of inter-  
 1112 nals waves generated by ocean storms. *Oceanography*, 25, 30–41. doi: 10.5670/  
 1113 oceanog.2012.39
- 1114 Sun, D., Bracco, A., Barkan, R., Berta, M., Dauhajre, D., Molemaker, M. J., ...  
 1115 McWilliams, J. C. (2020). Diurnal cycling of submesoscale dynamics: La-  
 1116 grangian implications in drifter observations and model simulations of the  
 1117 Northern Gulf of Mexico. *Journal of Physical Oceanography*, 50, 1605–1623.  
 1118 doi: 10.1175/JPO-D-19-0241.1
- 1119 Sun, W.-Y., & Sun, O. M. (2020). Inertia and diurnal oscillations of Ekman layers  
 1120 in atmosphere and ocean. *Dynamics of Atmospheres and Oceans*, 90, 101144.  
 1121 doi: 10.1016/j.dynatmoce.2020.101144
- 1122 Thoppil, P. G., Richman, J. G., & Hogan, P. J. (2011). Energetics of a global ocean  
 1123 circulation model compared to observations. *Geophysical Research Letters*,  
 1124 38(15). doi: 10.1029/2011GL048347
- 1125 Thyng, K. M., Greene, C. A., Hetland, R. D., Zimmerle, H. M., & DiMarco, S. F.  
 1126 (2016). True colors of oceanography: Guidelines for effective and accurate  
 1127 colormap selection. *Oceanography*, 29, 9–13. doi: 10.5670/oceanog.2016.66
- 1128 Timko, P. G., Arbic, B. K., Richman, J. G., Scott, R. B., Metzger, E. J., & Wall-  
 1129 craft, A. J. (2013). Skill testing a three-dimensional global tide model to  
 1130 historical current meter records. *Journal of Geophysical Research Oceans*, 118,  
 1131 6914–6933. doi: 10.1002/2013JC009071
- 1132 Torres, H. S., Klein, P., Menemenlis, D., Qiu, B., Su, Z., Wang, J., ... Fu, L.-  
 1133 L. (2018). Partitioning ocean motions into balanced motions and inter-  
 1134 nal gravity waves: A modeling study in anticipation of future space mis-  
 1135 sions. *Journal of Geophysical Research: Oceans*, 123(11), 8084–8105. doi:

- 1136 10.1029/2018JC014438
- 1137 Trossman, D. S., Arbic, B. K., Straub, D. N., G, R. J., Chassignet, E. P., Wallcraft,  
1138 A. J., & Xu, X. (2017). The role of rough topography in mediating impacts  
1139 of bottom drag in eddying ocean circulation models. *Journal of Physical  
1140 Oceanography*, *47*, 1941–1959. doi: 10.1175/JPO-D-16-0229.1
- 1141 Wang, J., Fu, L.-L., Qiu, B., Menenemlis, D., Farrar, J. T., Chao, Y., ... Flexas,  
1142 M. M. (2018). An observing system simulation experiment for the calibra-  
1143 tion and validation of the Surface Water Ocean Topography sea surface height  
1144 measurement using in situ platforms. *Journal of Atmospheric and Oceanic  
1145 Technology*, *35*. doi: 10.1175/JTECH-D-17-0076.1
- 1146 Wang, Y., Xu, Z., Hibiya, T., Yin, B., & Wang, F. (2021). Radiation path of diurnal  
1147 internal tides in the Northwestern Pacific controlled by refraction and inter-  
1148 ference. *Journal of Geophysical Research: Oceans*, *126*, e2020JC016972. doi:  
1149 10.1029/2020JC016972
- 1150 Waterhouse, A. F., MacKinnon, J. A., Nash, J. D., Alford, M. H., Kunze, E., Sim-  
1151 mons, H. L., ... Lee, C. M. (2014). Global Patterns of Diapycnal Mixing  
1152 from Measurements of the Turbulent Dissipation Rate. *Journal of Physical  
1153 Oceanography*, *44*(7), 1854–1872. doi: 10.1175/JPO-D-13-0104.1
- 1154 Wunsch, C. (1997). The vertical partition of oceanic horizontal kinetic en-  
1155 ergy. *Journal of Physical Oceanography*, *27*, 1770–1794. doi: 10.1175/  
1156 1520-0485(1997)027<1770:TVPOOH>2.0.CO;2
- 1157 Yu, X., Ponte, A. L., Eliot, S., Menenemlis, D., Zaron, E. D., & Abernathey, R.  
1158 (2019). Surface kinetic energy distributions in the global oceans from a high-  
1159 resolution numerical model and surface drifter observations. *Geophysical  
1160 Research Letters*, *46*(16), 9757–9766. doi: 10.1029/2019GL083074
- 1161 Zaron, E. D. (2017). Mapping the nonstationary internal tide with satellite altim-  
1162 try. *Journal of Geophysical Research Oceans*, *122*, 539–554. doi: 10.1002/  
1163 2016JC012487
- 1164 Zaron, E. D., & Egbert, G. D. (2014). Time-variable refraction of the internal tide  
1165 at the Hawaiian Ridge. *Journal of Physical Oceanography*, *44*, 538–557. doi:  
1166 10.1175/JPO-D-12-0238.1
- 1167 Zaron, E. D., & Eliot, S. (2021). An assessment of global ocean barotropic tide  
1168 models using geodetic mission altimetry and surface drifters. *Journal of Physi-  
1169 cal Oceanography*, *51*, 63–82. doi: 10.1175/JPO-D-20-0089.1